Not just a protein machine: how ribosomes regulate immune response

Dopler-Zandavalle, A.

Chapter 4

P-stalk ribosomes act as master regulators of cytokine-mediated processes

Anna Dopler, Ferhat Alkan, Yuval Malka, Rob van der Kammen, Kelly Hoefakker, Daniel Taranto, Naz Kocabay, Iris Mimpen, Christel Ramirez, Elke Malzer, Olga I. Isaeva, Mandy Kerkhoff, Anastasia Gangaev, Joana Silva, Sofia Ramalho, Liesbeth Hoekman, Maarten Altelaar, Roderick Beijersbergen, Leila Akkari, Jonathan Wilson Yewdell, Pia Kvistborg, William James Faller

Cell, 2024
https://doi.org/10.1016/j.cell.2024.09.039

Highlights

•Cytokines reshape the ribosome by regulating P-stalk incorporation
•P-stalk ribosomes are required for the alert-state cells to adopt upon cytokine exposure
•The preferential translation of cytokine-responsive mRNAs drives the alert state
•Incorporation of the P-stalk is partially regulated by TGF-β-mediated phosphorylation

Abstract

Inflammatory cytokines are pivotal to immune responses. Upon cytokine exposure, cells enter an “alert state” that enhances their visibility to the immune system. Here, we identified an alert-state subpopulation of ribosomes defined by the presence of the P-stalk. We show that P-stalk ribosomes (PSRs) are formed in response to cytokines linked to tumor immunity, and this is at least partially mediated by P-stalk phosphorylation. PSRs are involved in the preferential translation of mRNAs vital for the cytokine response via the more efficient translation of transmembrane domains of receptor molecules involved in cytokine-mediated processes. Importantly, loss of the PSR inhibits $CD8^+$ T cell recognition and killing, and inhibitory cytokines like transforming growth factor β (TGF-β) hinder PSR formation, suggesting that the PSR is a central regulatory hub upon which multiple signals converge. Thus, the PSR is an essential mediator of the cellular rewiring that occurs following cytokine exposure via the translational regulation of this process.

Graphical Abstract [figure on the next page]

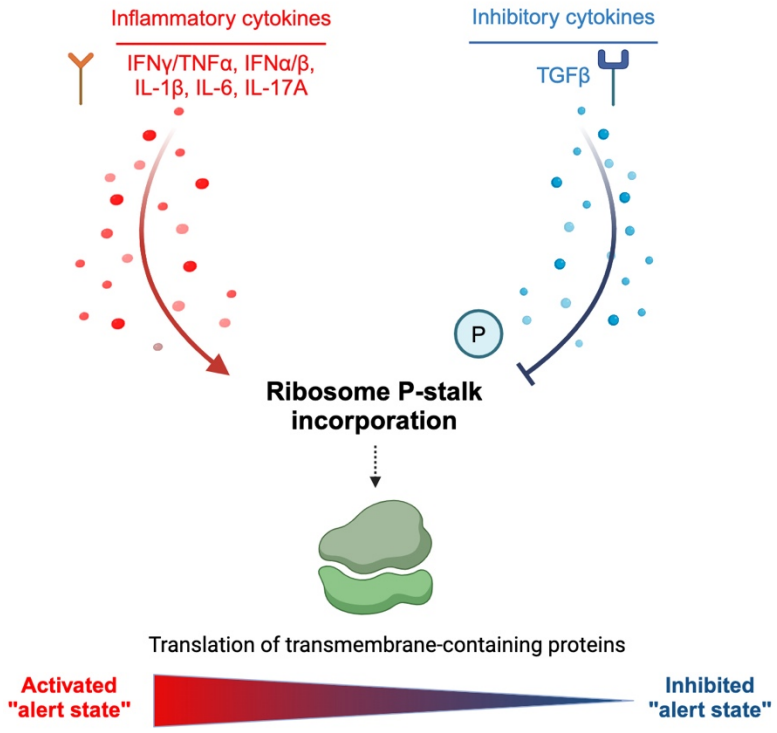

Summary

Immune evasion is a well-known occurrence in cancer cells and has been included as one of the new hallmarks of cancer [1]. The success of immune checkpoint blockade (ICB) in several cancer types has highlighted the importance of immune surveillance in tumor control; however, the majority of patients either do not respond or acquire resistance to such therapies [2]. It is well established that the infiltration of T cells in the tumor microenvironment (TME) is a critical mediator of ICB [3]. While T cells directly kill tumor cells, they also secrete cytokines such as interferon-γ (IFNγ) and tumor necrosis factor alpha (TNF-α), and as a result, human tumors often show evidence of transcriptional signatures of IFNγ signaling [4]. While IFNγ signaling serves as a useful biomarker of ICB response [5], it also leads to a major rewiring of tumor cell and immune cell behavior [6]. Upon cytokine exposure, cells take on an alert state that is characterized by an upregulation of chemokines and checkpoints, an increase in antigen processing and presentation (APP) [7], and in some cases, the onset of senescence or apoptosis [8]. Conversely, inhibitory cytokines like transforming growth factor β (TGF-β) do the opposite, as can be seen in tumors with a dominant immunosuppressive myeloid cell population [9].

However, despite this major rewiring and the significant phenotypic consequence of it, our understanding of how cytokines modify tumor behavior is still lacking. Analysis of cytokine responses has tended to focus on transcriptional regulation, and while some examples of post-transcriptional regulation of cytokine responses exist [10-12], there is still much to learn in this context.

The concept of ribosomal populations with specific functions has been around for more than 20 years [13,14], but it remains controversial. Recent work has clearly shown more variability to the ribosome than has previously been appreciated [15,16], and this supports the potential of specialized functions [17-20]. Many members of the translation machinery are selectively regulated [21], and considering its complexity, it is not difficult to imagine the ribosome itself being similar. The stoichiometry of ribosomal proteins (RPs) has been of particular interest in this context [16,22], and RPs are known to be important for T cell survival and development [23-25], dendritic cell (DC) activation [26], and B cell activation [27], demonstrating that they play a role in immune responses. Indeed, the “immunoribosome” is a hypothesized subset of ribosomes that selectively generates antigenic peptides [28]. Recent evidence has supported a role for RPs in this context [29], suggesting that ribosomes may play an unappreciated role in responses to cytokine exposure.

Based on this, we speculated the existence of a post-transcriptional mechanism of cytokine-induced cellular rewiring, mediated by a change in the ribosome. Such a regulator of cytokine responses would be of critical importance for our understanding of immune regulation in patient response to ICB. Here, we identify such a cytokine-responsive alert-state ribosome population, defined by the presence of the P-stalk, and show that these P-stalk ribosomes (PSRs) are a critical mediator of the cellular rewiring that occurs following cytokine exposure, via the translational regulation of this process.

Results

The P-stalk defines a cytokine-responsive alert-state ribosome

To identify RPs that regulate tumor cell response to cytokines, we treated human melanoma cells (Mel624 and M026 cell lines) with IFNγ and TNF-α. We then performed proteomic analysis of actively translating ribosomes to identify RPs that change in response to treatment (Figure 1A). We confirmed that the cells took on a cytokine-induced alert state by measuring both APP activation by increased human leukocyte antigen (HLA) I cell surface expression

(determined via flow cytometry) and the expression of immunoproteasome subunits (determined by proteomics; Figures S1A–S1D). We then used sucrose density gradient centrifugation to isolate the actively translating ribosomes from these cells. We also collected total protein and compared cytoplasmic RP levels to those in the translating ribosomes using LC-mass spectrometry (MS). This analysis revealed that in both cell lines, P1 was the protein with the largest increase in the translating ribosomes (Figure 1B). We confirmed this increase by measuring polysome, sub-polysome, and total P1 levels by immunoblotting, which confirmed that P1 is significantly increased in polysomes (actively translating ribosomes) following IFNγ/TNF-α exposure. Crucially, another RP, uL30, does not increase, demonstrating that this is not a general effect on the ribosome (Figure 1C).

P1 forms a heterodimer with P2, and two of these heterodimers are anchored to the ribosome via uL10. This pentameric stalk (also known as the P-stalk) is the central component of the GTPase-associated center of the ribosome [30]. Interestingly, the P1/P2 heterodimer has long been known not to be essential for translation [31], and, unlike most other RPs, dynamically associates with the ribosome [32]. To understand whether the cytokine-mediated changes we have detected are P1 specific, or rather a result in an increase in the P-stalk, we tested whether P2 is also increased in translating ribosomes following cytokine treatment. Despite not identifying it in our proteomic analysis, western blotting showed that this is indeed the case (Figure 1C), suggesting that the addition of the P1/P2 heterodimer to the ribosome is increased following IFNγ/TNF-α exposure.

IFNγ and TNF-α are just two of the cytokines known to regulate the alert state. Additional experiments revealed that other immune-activating cytokines, including IFNα/IFNβ, interleukin-1β (IL-1β), IL-6, and IL17-A, also increase PSR abundance (Figures S1E and S1F), suggesting that the PSR is activated regardless of the inflammatory signal. We also treated the cells with an immune inhibitory cytokine (TGF-β), which showed that P-stalk incorporation is decreased by TGF-β (Figure 1D).

We confirmed these findings in cell lines from diverse origins (ovarian cancer [SK-OV-3], colorectal cancer [HCT 116], and immortalized retinal pigment epithelial cells [hTERT-RPE1]) (Figures S1G–S1I), demonstrating that a change in ribosomes in response to cytokines is consistent across tissues. These results suggest that the PSR may be a regulatory node upon which multiple signals converge and that it may therefore act as a general regulator of cytokine-mediated processes.

Figure 1

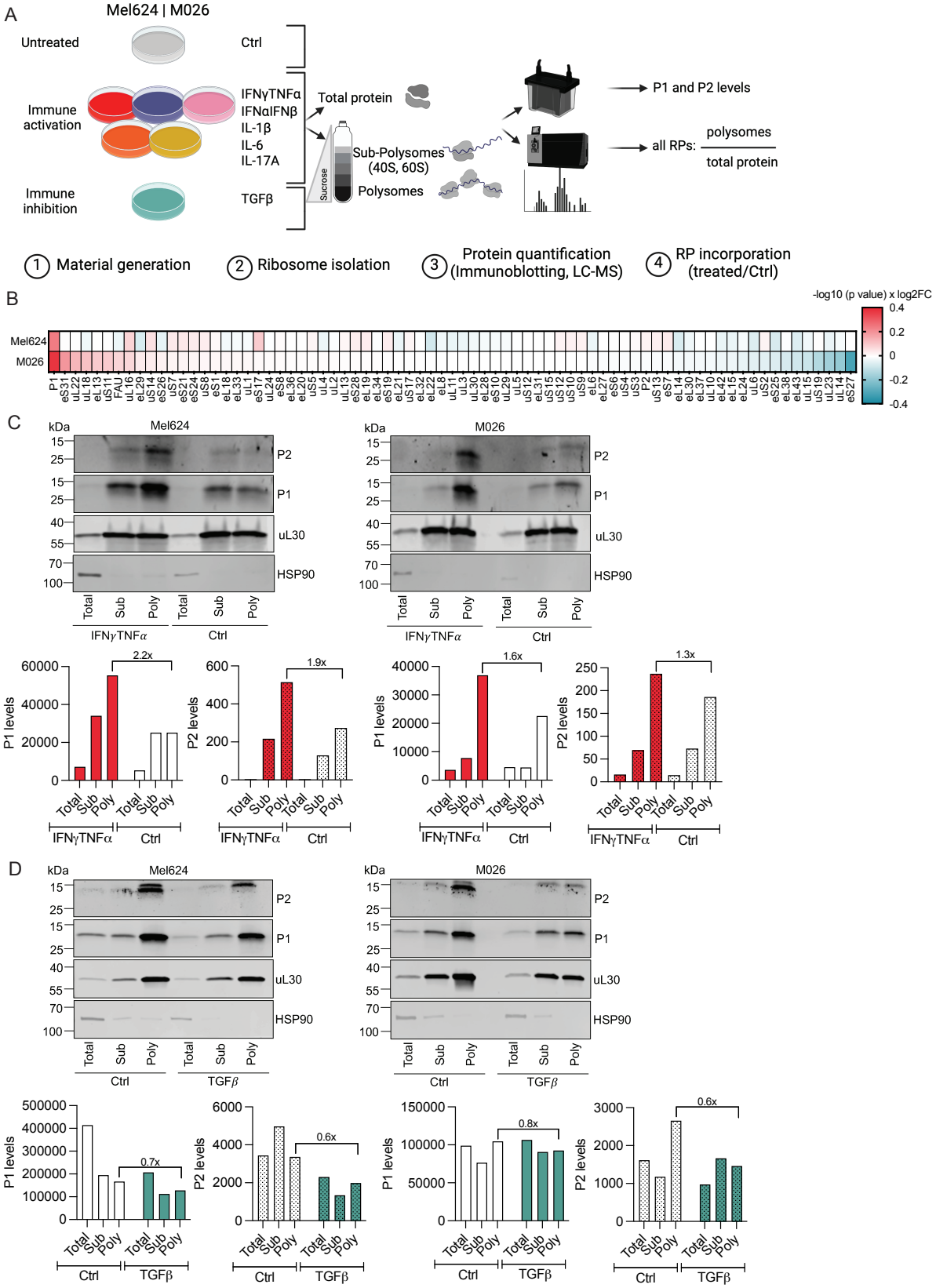

Figure 1. [legend on the next page]

Figure 1 [previous page]. The P-stalk defines a cytokine-responsive ribosome subpopulation
(**A**) Schematic representation of experimental setup.
(**B**) P1 association with the translating ribosome (poly) is increased upon IFNγ/TNF-α exposure in Mel624 and M026 tumor cells. Heatmap shows polysome to total ratio in cytokine-treated vs. untreated cells. *n* = 3 independent experiments.
(**C**) Western blot analysis confirming increased polysomal association of P1 and P2 upon IFNγ and TNF-α exposure. HSP90 was used as loading control, and uL30 was used as control RP for data normalization. *n* = 1 experiment per cell line.
(**D**) TGF-β inhibits formation of the PSR. Western blot analysis showing decreased polysomal association of P1 and P2 following TGF-β exposure. HSP90 was used as loading control, and uL30 was used as control RP where no changes could be observed. *n* = 1 experiment per cell line.
See also Figure S1.

The PSR regulates APP

To measure whether the PSR is important for cytokine-mediated processes, we used short hairpin RNA (shRNA) to knockdown (KD) P1 in both melanoma cell lines, using independent shRNAs (shP1#1, shP1#3). We also used an shRNA against a control RP that was unresponsive to cytokine treatment (shL28) and two scrambled control shRNAs (shCtrl#1, shCtrl#2). Transduction efficiency was measured using mCherry (%) expression and was approximately 90% across cell lines (Data S1). KD efficiency was variable across hairpins and cell lines, with the Mel624 cell line showing 42% and 50% KD for shP1#1 and shP1#3, and the M026 cell lines showing 28% and 16% KD, respectively (Data S1). Interestingly, the strength of the phenotypes presented in the remainder of this manuscript somewhat correlate with the strength of P1 KD, with the Mel624 cell line regularly providing more reliable results, particularly compared with the M026 shP1#3 cell line, which shows poor KD (16% KD).

In order to investigate the functional relevance of the PSR, we assessed several well-defined processes. We initially measured whether the PSR downregulation via P1 KD reduced APP in cells without cytokine exposure. This was indeed the case, and loss of the PSR resulted in a strong and significant decrease of both pan class I (using an HLA-A, -B, or -C-specific antibody) and HLA-A2 cell surface expression compared with cells infected with shL28 or a scrambled control (Figures 2A and S2A). We also measured surface levels of HLA-B and HLA-C individually upon loss of the PSR, which resulted in strong and significant decrease of both markers (Figure S2B). We then measured the ability of these cells to recover their surface HLA I after acid-mediated removal and found that while the kinetics of recovery were similar, the magnitude was significantly reduced following P1 KD, as would be expected in cells with reduced HLA I levels (Figure S2C). We next treated the cells with IFNγ/TNF-α and measured

their ability to take on the alert state via the upregulation of HLA I cell surface expression. While all cells showed an increase in cell surface HLA I, that increase was significantly attenuated in shP1 cells compared with shL28 or scrambled controls (Figures 2B, S2D, and S2E). To ensure this was specific to P-stalk-containing ribosomes, we also measured HLA levels upon cytokine exposure following KD of uL30, eS10, and eS28, none of which showed the same attenuation (Figures S2F and S2G). Additionally, we have shown that TGF-β treatment inhibits PSR formation via decreased P-stalk incorporation (Figure 1D). In line with this, TGF-β treatment also reduced HLA I cell surface expression (Figures 2C and S2H).

We then carried out a melanoma cell/T cell co-culture assay [33]. This assay is based on donor $CD8^+$ T cells retrovirally transduced with a T cell receptor (TCR) specific for HLA-A2 restricted peptides derived from MART-1 or NY-ESO-1, both of which are presented by Mel624 and M026 tumor cells. If antigens are correctly presented, they will be recognized by T cells, resulting in their activation (measured by IFNγ and TNF-α production and CD107a cell surface expression) and the killing of the tumor cells. While KD of eL28 did not affect T cell recognition, KD of P1 resulted in a strong and significant decrease in recognition by both MART-1 and NY-ESO-1-specific $CD8^+$T cells (Figures 2D, S3A, and S3B). A live imaging killing assay confirmed this finding, with shP1-expressing cells being far less efficiently killed by T cells compared with either shL28 or a scrambled control (Figures 2E and S3C).

Although our data suggested this effect was not a result of a general dysfunction of the ribosome (Figure S2G), we measured whether P1 KD resulted in the reduced expression of the source proteins from which the antigens derive. However, the levels of MART-1 and NY-ESO-1 were largely unchanged in shP1 cells (Figure S3D), discounting this possibility, although P1 KD did reduce both protein synthesis (Figure S4A) and proliferation (Figure S4B). We next inhibited protein synthesis to the same degree by knocking down another RP, eL6 (Figure S4C). This intervention did not cause a decrease in HLA I cell surface expression, consistent with the conclusion that the effect of the PSR is not based on its effect on global protein synthesis (Figure S4D). Additionally, as the P-stalk has been shown to regulate GCN2 activation [34], we also measured the levels of phosphorylated eIF2α in both cell lines. These data showed no difference in eIF2α phosphorylation following P1 KD, either with or without IFNγ/TNF-α treatment (Figure S4E), suggesting that this role of the P-stalk is not relevant following cytokine exposure.

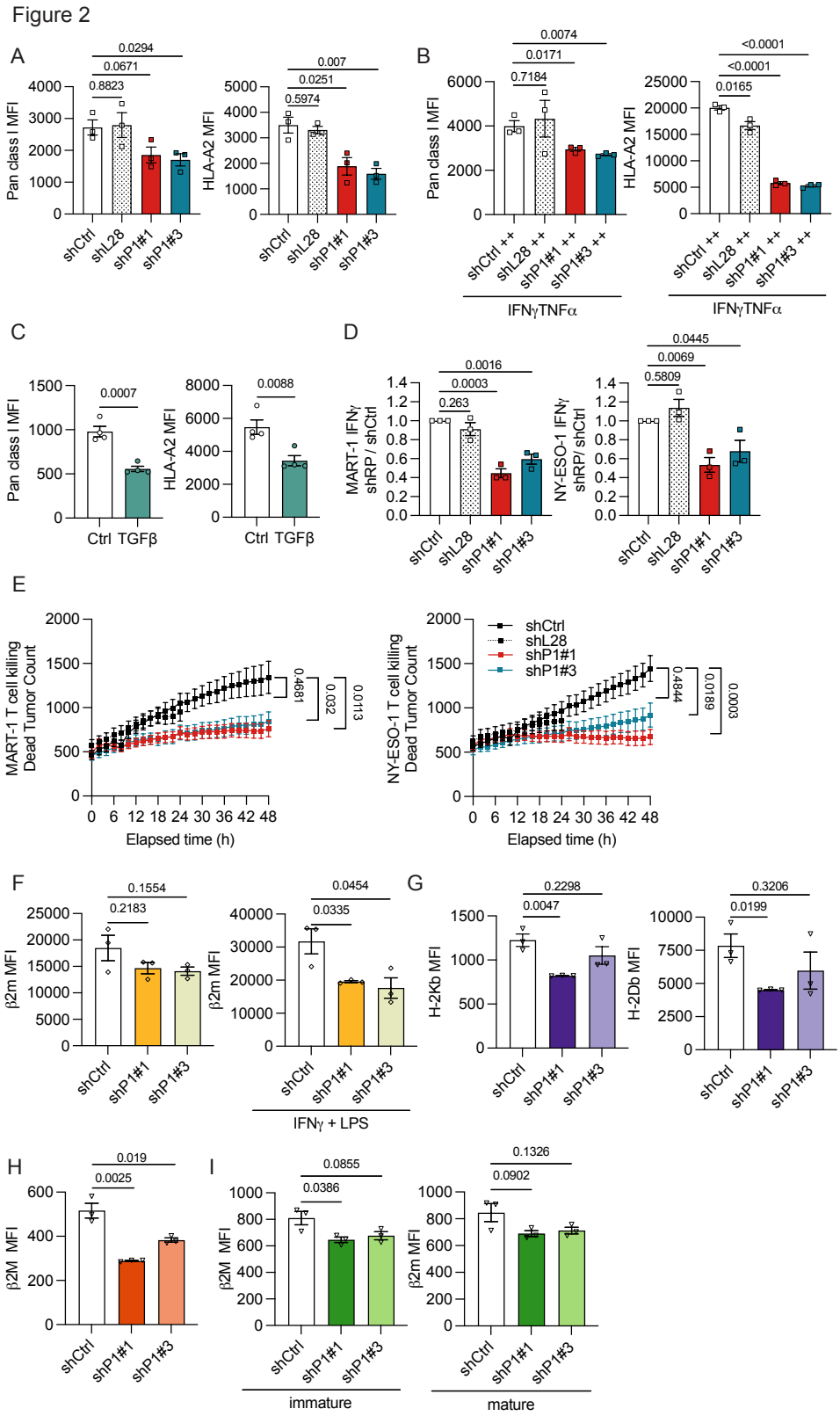

Figure 2. [legend on the next page]

Figure 2 [previous page]. The PSR regulates APP across cell types and tissues

(**A**) P1 KD decreases HLA I surface levels. HLA levels were assessed by flow cytometry using the MFI. *n* = 3 independent experiments, each assessed in triplicates. Data are represented as mean ± SEM, and *p* values were determined using a two-tailed t test.

(**B**) Exposure to IFNγ/TNF-α results in low basal HLA I surface levels in shP1 compared with control tumor cells. *n* = 3 biological replicates represented as mean ± SEM. *p* values were calculated using a two-tailed t test.

(**C**) TGF-β decreases HLA I surface levels. HLA levels were assessed by flow cytometry using the MFI. *n* = 4 biological replicates. Data are represented as mean ± SEM, and *p* values were determined using a two-tailed t test.

(**D**) MART-1 and NY-ESO-1-specific $CD8^+$ T cell recognition is decreased in shP1 tumor cells compared with control cells. *n* = 3 independent experiments, each assessed in triplicates. Data are represented as mean ± SEM, and *p* values relative to shCtrl were determined using a two-tailed t test.

(**E**) MART-1 and NY-ESO-1-specific $CD8^+$ T cell killing is suppressed in shP1 tumor cells. *n* = 3 independent experiments, each assessed in triplicates. Data represent mean and error ± SEM, and *p* values were calculated with a two-tailed t test.

(**F**) P1 KD decreases β2m surface levels in PBMC-derived human macrophages, with and without activation (IFNγ + LPS). β2m levels were assessed by flow cytometry using the MFI. *n* = 3 biological replicates. Data are represented as mean ± SEM, and *p* values were determined using a two-tailed t test.

(**G**) P1 KD decreases H-2Kb and H-2Db surface levels in B16 mouse melanoma cells. H-2Kb and H-2Db levels were assessed by flow cytometry using the MFI. *n* = 3 independent experiments. Data are represented as mean ± SEM, and *p* values were determined using a two-tailed t test.

(**H**) P1 KD decreases β2m surface levels in mouse bone marrow-derived macrophages (BMDMs). β2m levels were assessed by flow cytometry using the MFI. *n* = 3 biological replicates. Data are represented as mean ± SEM, and *p* values were determined using a two-tailed t test.

(**I**) P1 KD decreases β2m surface levels in immature and mature mouse bone marrow-derived dendritic cells (BMDCs). β2m levels were assessed by flow cytometry using the MFI. *n* = 3 biological replicates. Data are represented as mean ± SEM, and *p* values were determined using a two-tailed t test.

See also Figures S2 and S3.

PSR function is conserved across cell types and species

To explore the clinical relevance of our findings, we turned to the TCGA database [35]. RPs tend to be co-regulated, so we therefore ranked samples based on P1 or P2 expression relative to the expression of other RPs, thus controlling for globally high/low RP expression and enabling us to focus on samples whose P1 or P2 levels are higher than other RPs. This analysis showed that high P1 or P2 levels (relative to other RPs) significantly positively correlated with an IFNγ signature [36] and an effector $CD8^+$ T cell signature [4] in melanoma.

Crucially, we did not observe the same correlation when other RPs were analyzed in the same manner (Figures S4F and S4G). Further analysis of TCGA data revealed the same significant correlation in the majority of cancer types (24 of 36), suggesting that the P-stalk regulates cytokine responses in diverse tissues (Figure S4H).

To further understand the relevance of the PSR, we assessed primary human professional antigen-presenting cells (APCs). We isolated $CD14^+$ monocytes from human peripheral blood mononuclear cells (PBMCs) derived from buffy coats and differentiated them into macrophages (BMDMs), or DCs. We then knocked down P1 (Figure S5A); however, while we successfully generated modified macrophages, P1 KD in DCs proved impossible, and we proceeded with the macrophages alone. We then measured antigen presentation both with and without activation (via treatment with IFNγ and LPS). Unlike the cell lines that we had already characterized, we did not know the HLA haplotype of the primary cells, and we therefore used an antibody to β_2M to quantify APP. This showed that loss of the PSR substantially reduces APP in primary macrophages, particularly following activation (Figure 2F).

As the ribosome is a highly conserved macromolecular complex, we also tested whether this mechanism of APP regulation was present in mouse tissue. First, we knocked down P1 in the mouse B16 melanoma cell line (Figure S5B) and measured H-2Kb and H-2Db cell surface expression, as these are the MHC I alleles known to be expressed by this cell line. P1 KD resulted in a decrease in the cell surface expression of both alleles (Figures 2G and S5C). We also isolated bone marrow-derived monocytes from mice and BMDMs or DCs (BMDCs). Unlike their human equivalent, we successfully knocked down P1 in mouse DCs as well as macrophages (Figures S5D and S5E) and quantified APP using an antibody to β_2M. Again, P1 KD significantly decreased APP in both cell types, confirming that the PSR also exists in mouse cell lines and tissue (Figures 2H and 2I).

In all, these findings indicate that the loss of the PSR has a striking effect on the antigen-presenting ability of cells and, in the context of tumor cells, the ability of $CD8^+$ T cells to detect and kill them. Furthermore, it is conserved across tissues and exists in mice as well as humans.

The PSR preferentially translates mRNAs important for immunosurveillance

Following confirmation of the importance of the PSR, we next set out to understand how it works. Upon P1 KD, we first measured the intracellular protein levels of HLA I using a pan

class I-specific antibody. This showed that total HLA I protein levels were significantly decreased (Figure S5F). However, qPCR analysis did not reveal changes in mRNA levels (Figure S5G), suggesting post-transcriptional regulation. Isolation of ribosomal fractions from these cells using sucrose gradient density centrifugation showed that despite no change in HLA-A, -B, or -C mRNA levels, their polysomal association was significantly decreased following P1 deletion, showing that it is translationally regulated (Figure S5H).

To gain a more global view of the translatome of the PSR, we expressed a HA-tagged version of P1 in the Mel624 cell line, alongside a line expressing HA-tagged eL22 (Figure S5I). In fitting with its role as a regulator of APP, P1 overexpression was sufficient to increase HLA levels, an effect not seen upon eL22 overexpression (Figures 3A and S5I). These tags then allowed us to specifically isolate P1- and eL22-containing ribosomes following IFNγ/TNF-α exposure and characterize the associated mRNAs via ribosome profiling. Immunoblotting confirmed enrichment of the HA tag following immunoprecipitation (Figure S5J), while analysis of the resulting ribosome profiling confirmed a 29–30 nucleotide read length and 3-nucleotide periodicity in these data (Data S1). These data showed that alongside HLA I, the mRNAs of many other components of the APP machinery were preferentially associated with the PSR, including TAP1, TAP2, and TAPBP (Figure 3B). Additionally, key chemokines (including CXCL1 and 9) were enriched on the PSR, as were other cytokine-regulated mRNAs, including a central regulator of T cell recruitment (ICAM1) [37], while a negative regulator of TNF-α-mediated apoptosis (TNFAIP3) [38] was depleted (Figure 3B). For context, while the APP group makes up 0.6% of the detected translatome (18 of 2,993 genes), it makes up 7.5% of the enriched translatome (10 of 132 genes). In line with this, P1 KD resulted in a decrease of the IFNγ receptor and, to a lesser degree, TNF-α receptors on the cell surface (Figures S6A and S6B). Interestingly, this decrease did not appear to affect the signaling downstream of IFNγ/TNF-α, as measured by STAT1 phosphorylation (Figure S6C). In all, these data suggest that the entire cytokine response is regulated by the PSR.

Figure 3

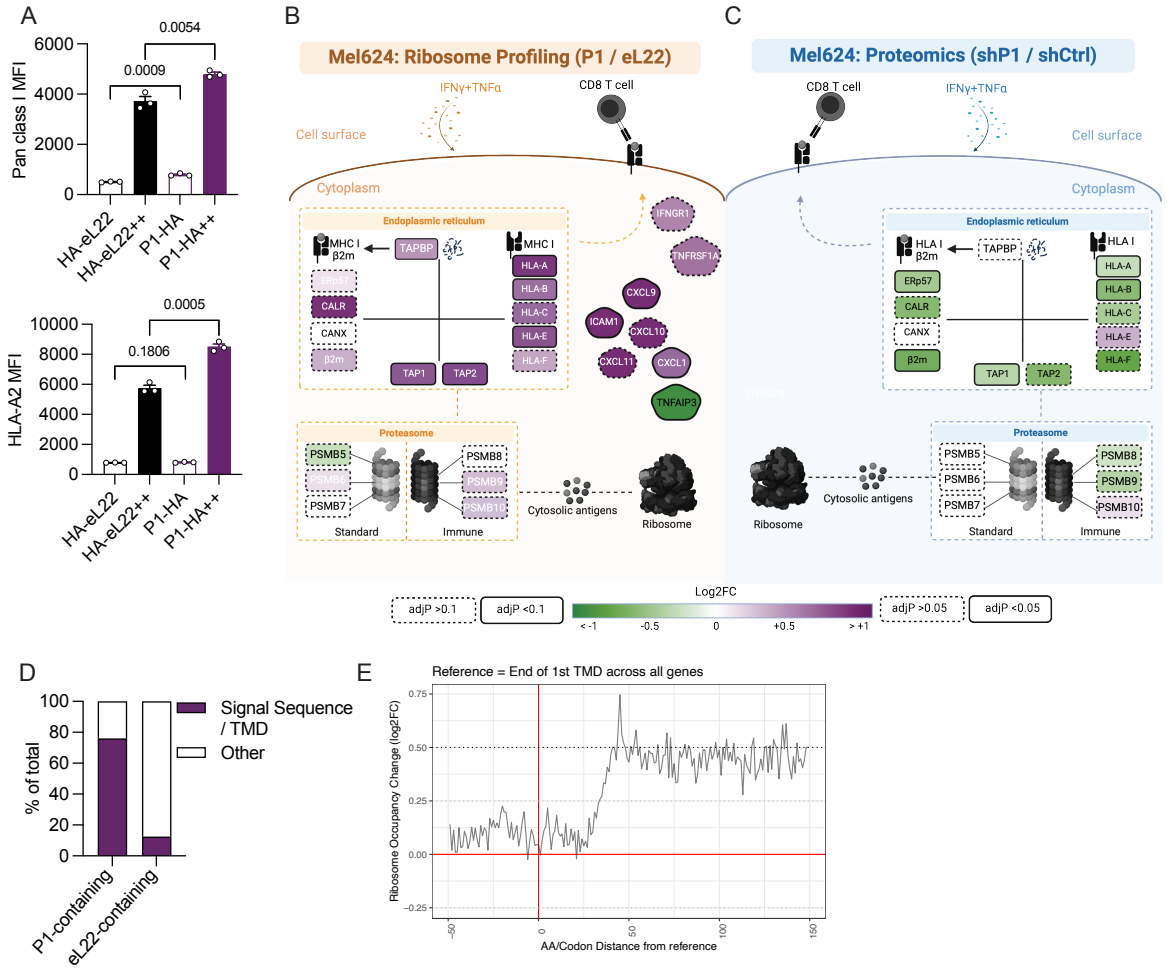

Figure 3. The PSR preferentially translates mRNAs important for immunosurveillance

(**A**) PSR overexpression increases HLA I surface levels in untreated (P1-HA, HA-eL22) and IFNγ/TNF-α treated (P1-HA++, HA-eL22++) tumor cells. HLA levels were assessed by flow cytometry using the MFI. *n* = 3 independent experiments. Data are represented as mean ± SEM, and *p* values were determined using a two-tailed t test.

(**B**) Ribosome profiling reveals preferential translation of HLA and other APP components by the PSR. The PSR also preferentially translates key chemokines and other cytokine-responsive mRNAs important for immune response. *n* = 2 biological replicates per condition, and *p* values were calculated using the DESEQ2 package.

(**C**) Proteomics analysis reveals downregulation of HLA and other APP components upon P1 KD and IFNγ/TNF-α exposure. *n* = 3 independent experiments, and *p* values were calculated using a two-tailed t test.

(**D**) mRNAs that are preferentially translated by PSRs are enriched for coding signal peptide and/or transmembrane domains.

(**E**) The PSR is specifically enriched at translating mRNA regions that come after the translation of the first transmembrane domain. The plot shows the aggregated ribosome occupancy differences (PSR vs.

all ribosomes) at each codon distance from the reference set, ends of the first TMD domain across all genes.
See also Figures S4, S5, and S6.

Extending these findings, we carried out a proteomic analysis of shP1 cells compared with shCtrl cells, with and without activation. These data also showed that the protein levels of multiple APP components were decreased following P1 KD (Figures 3C, S6D, and S6E). Furthermore, gene set enrichment analysis (GSEA) showed that genesets associated with antigen presentation and HLA I were among the most downregulated following P1 KD (Figure S6F), confirming that multiple members of this process are regulated in the same manner as HLA I.

In order to understand the mechanism by which the PSR regulates specific mRNAs, we analyzed the ribosome profiling data in more detail. Annotation of the sequence features enriched on mRNAs associated with the PSR revealed that messages translated at the ER were substantially enriched. While 12.5% of eL22-enriched mRNAs contained a signal sequence or a transmembrane domain (TMD), 76% of P1-enriched messages contained them (Figure 3D). Visualization of the distribution of sequencing reads on TMD-containing mRNAs revealed that P1-containing ribosomes were significantly enriched after the first TMD (Figure 3E), suggesting that the role of the P-stalk in elongation may be causing differential translation of specific mRNAs [39,40]. It has previously been reported that the P-stalk is required for dengue viral replication [41], as it appears to be needed to relieve ribosome pausing on the viral RNA [42]. The same study suggested that the P-stalk aids in TMD translation due to pauses that are thought to occur on such sequences [42], potentially explaining the observed findings.

PSR activation and inhibition show different dynamics

In order to get a deeper understanding of the activation and inhibition of the PSR, we measured the dynamics of P-stalk incorporation following cytokine exposure. We have previously shown that total levels of P1 and P2 do not change (Figure 1C), and we confirmed that they are not transcriptionally upregulated upon exposure (Figure S7A). We therefore treated cells with IFNγ/TNF-α for 1, 6, 12, 24, and 48 h and measured P-stalk incorporation. This revealed that incorporation does not increase until 48 h after cytokine exposure (Figures 4A and S7B), which is in fitting with a transcription-based activation, perhaps via the expression of a chaperone or other regulator. We then carried out the same experiment following TGF-β exposure and surprisingly found that PSR deactivation (via P-stalk removal)

was an extremely rapid process, with decreased P-stalk proteins detectable just 1 h after TGF-β exposure (Figures 4B and S7C).

The speed of PSR deactivation suggests that it may be mediated by a post-transcriptional mechanism. Interestingly, the P-stalk proteins are known to be phosphorylated, and while the function of this modification on P1 and P2 is unknown, it has been suggested that phosphorylation of the third P-stalk protein (uL10) regulates its association with the ribosome [43,44]. As these phosphorylation sites are conserved among all three P-stalk members [43], it is reasonable to consider that modification of P1 and P2 may also be regulating their ribosome association. We therefore carried out a phospho-proteomic analysis of the M026 cell line, with and without IFNγ/TNF-α. These data showed that there is a loss of phosphorylation upon treatment, suggesting that this is an inhibitory modification (Figure 4C).

We therefore edited the endogenous P2 locus to generate cell lines that cannot be phosphorylated on the conserved sites (S102/S105). We created two distinct P2 phospho-dead clones and associated controls, but unfortunately, due to unfavorable sequences, the same could not be done for P1. As we hypothesized that these are inhibitory phosphorylations, we treated the cells with TGF-β and measured the incorporation of P1 and P2 into the ribosome. In fitting with an inhibitory role, phospho-mutation of these sites increased basal P-stalk incorporation (Figure 4D). Furthermore, the decrease in incorporation seen following TGF-β exposure was attenuated in one clone and abolished in the other, demonstrating that TGF-β-mediated phosphorylation regulates the PSR via altered P-stalk incorporation (Figures 4D and S7D). We then measured APP in the same context, which showed that the P2 phospho-dead mutants maintained high cell surface HLA I levels in the presence of TGF-β, confirming the phospho-regulation of the PSR (Figure 4E). We also tried to generate a phospho-mimetic cell line; however, these cells were not viable. This is not unexpected, as chronic TGF-β treatment, which we hypothesize would phosphorylate P-stalk proteins, is toxic for cells. Interestingly, P2 phospho-dead cell lines were more resistant to this chronic treatment, further underscoring the role of P2 phosphorylation in TGF-β-mediated phenotypes (Figure S7E).

Figure 4

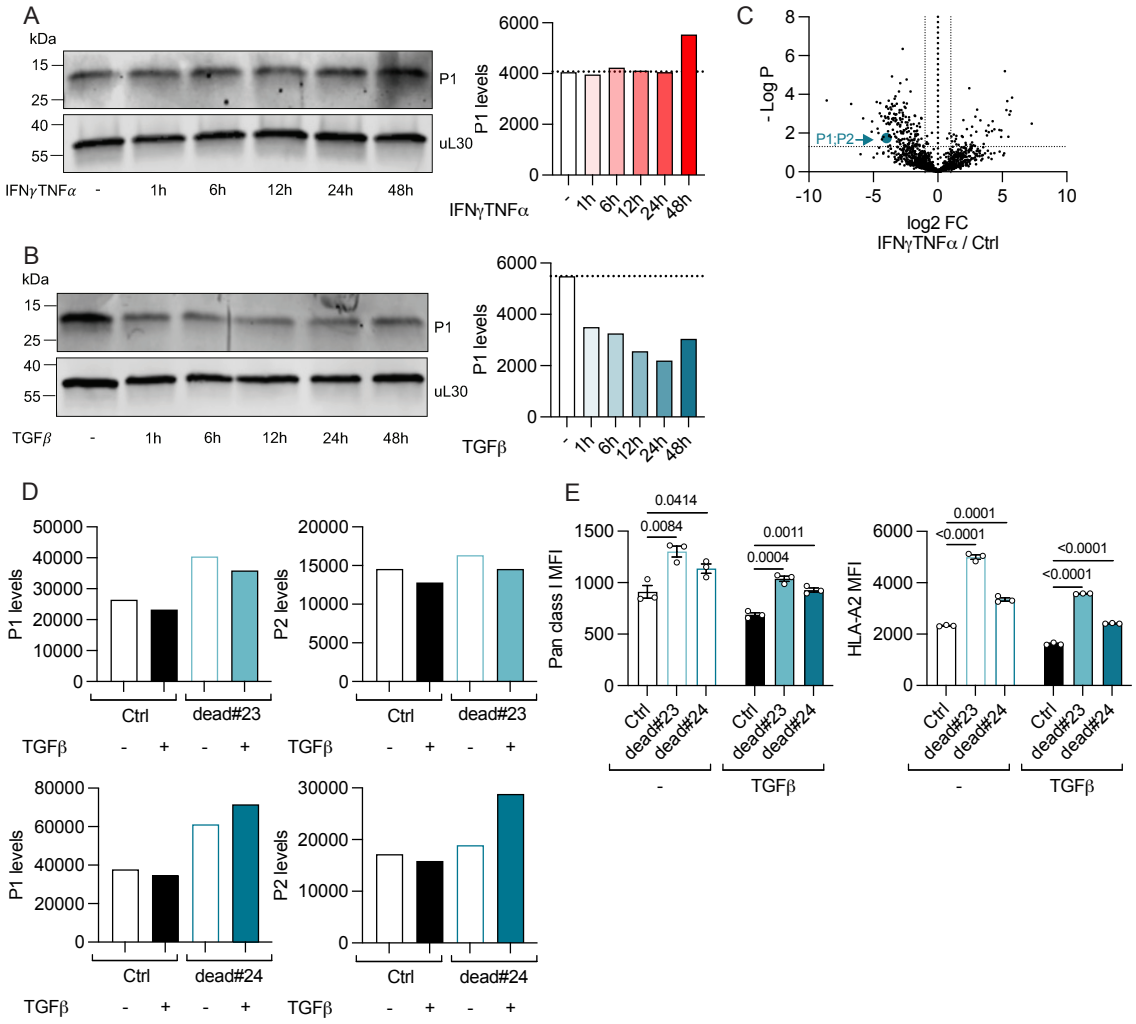

Figure 4. PSR activation and inhibition show different dynamics

(**A**) Western blot analysis confirming PSR formation after 48 h of IFNγ/TNF-α treatment. Polysomal association of P1 was measured in untreated tumor cells and tumor cells treated with IFNγ/TNF-α at indicated timepoints (1, 6, 12, 24, and 48 h). uL30 was used as control RP for data normalization. *n* = 1 experiment per cell line.

(**B**) Western blot analysis confirming PSR inhibition after 1 h of TGF-β treatment. Polysomal association of P1 was measured in untreated tumor cells and tumor cells treated with TGF-β at indicated timepoints (1, 6, 12, 24, and 48 h). uL30 was used as control RP for data normalization. *n* = 1 experiment per cell line.

(**C**) IFNγ/TNF-α exposure results in loss of P1/P2 phosphorylation in tumor cells. *n* = 3 independent experiments.

(**D**) Western blot analysis of P2 phospho-dead cell lines reveals TGF-β-mediated inhibition of the PSR by phosphorylation. Polysomal association of P1 and P2 was measured in control cells and two phospho-dead cell lines (#23 and #24) with or without TGF-β. uL30 was used as control RP for data

normalization. Additional comparisons are represented and quantified in Figure S7D (IFNγ/TNF-α vs. Ctrl, IFNγ/TNF-α + TGF-β vs. Ctrl). *n* = 1 experiment per cell line.
(**E**) TGF-β-mediated reduction of the APP is regulated by phosphorylation. HLA levels were assessed in control cells and two phospho-dead cell lines (#23 and #24) with or without TGF-β by flow cytometry using the MFI. *n* = 3 independent experiments. Data are represented as mean ± SEM, and *p* values were determined using a two-tailed t test.
See also Figure S7.

Discussion

It is well established that for the majority of cancers, the expression of chemokines and HLA I is strongly correlated with clinical response to checkpoint targeting therapies [45-47]. Indeed, many alterations that affect the "visibility" of a tumor are known to be mechanisms of cancer immune evasion, and the silencing of both chemokines and components of the APP machinery has been observed in human cancer [48-50]. As such, the discovery of a novel regulator of these genes is an important one.

Here, we show that first, the PSR is regulated by both pro- and anti-inflammatory cytokines, positioning it as a central nexus, upon which several signals converge; second, the PSR selectively translates many cytokine-responsive mRNAs, including APP components, chemokines, and other mRNAs that help rewire cells following cytokine exposure; third, this is regulated by phosphorylation; and fourth, this is a general mechanism across tissues, cancer types, and species.

The fact that the ribosome itself is at the center of this regulation is in fitting with recent reports of direct regulation of phenotypes by the ribosome [22, 51-53]. Indeed, it has previously been hypothesized that an immunoribosome exists [28], which was defined as a subset of ribosomes dedicated to translating DRiPs for HLA I immunosurveillance [13, 14], thus altering the antigen repertoire. However, the PSR plays a much broader role than this, translating the mRNA involved in multiple cytokine responses and acting as an alert-state ribosome, regulating not just APP but much of the cellular rewiring that occurs upon cytokine exposure. While the ribosome has not traditionally been considered a viable target for therapy due to its crucial role in biology, the recent identification of dynamic RP/ribosome interactions suggests that there may in fact be unrealized opportunities [52, 54]. Indeed, the P1/P2 stalk proteins were the first RPs shown to dynamically associate with ribosomes [55], highlighting them as interesting RPs in this context.

It remains to be fully determined why and how PSR preferentially translates specific mRNAs. Interestingly, it has been described previously that the ribosomal P-stalk is needed for the translation of transcripts encoding TMDs [42], and we see a similar effect here. As a result of their function, cytokine-responsive proteins are enriched for signal peptides and TMDs, such as HLA I and the TAP transporter proteins, which could at least partially explain the results described here. However, many signal peptide and TMD-containing mRNAs are not enriched on the PSR, suggesting that this is only part of the picture. Other potential explanations could include mRNA selection via the binding of specific RNA-binding proteins to mRNAs [56], or altered ribosome localization. An attractive hypothesis that links the PSR to the original concept of the immunoribosome is that the P-stalk localizes a subset of ribosomes to TAP-associated proteasomes to enable peptide channeling [57], but such additional mechanisms were not probed in this study.

Our discovery also raises several additional questions. We have shown that P-stalk incorporation into the ribosome is regulated by both inflammatory (IFNγ/TNF-α, IFNα/IFNβ, IL-1β, IL-6, and IL17-A) and inhibitory (TGF-β) cytokines, but we have not extensively tested the ability of all relevant cytokines to do the same. It will also be interesting to know how widespread this role of the PSR is. Our analysis of both mouse and human primary cells, as well as the TCGA datasets, suggests that cytokine response is regulated in this manner in a large number of tissues.

It is also key that we understand how specific this response is to cytokine exposure. Although the P-stalk is not essential for translation [31], it is known to play a key role in the recruitment of translation factors to the elongating ribosome [58-60]. P-stalk containing ribosomes obviously exist without cytokine exposure (although their number is modulated by cytokines; Figure 1), and our data show that they translate distinct mRNAs in basal conditions (Figure S6E). This suggests that although they clearly play a role in cytokine response, it may be part of a more general function. Cytokine-responsive mRNAs are largely translated at the ER, so it is possible that the P-stalk plays a role in SRP-mediated ribosome pausing [61]. We have shown that P-stalk-containing ribosomes are enriched following TMDs (Figure 3E). The pattern of this enrichment (coming around 30 amino acids following the end of the TMD) suggests that it happens as the TMD emerges from the ribosome and is folded, a situation known to induce ribosome stalling [42, 62, 63]. Considering the well-established role of the P-stalk in translation elongation [58, 59], it is not difficult to imagine that it plays a role in overcoming such stalls, a function that is unlikely to be restricted to cytokine-related mRNAs. It would be very interesting to assess the P-stalk-related translatome in other contexts,

particularly those that also involve an increase in translation at the ER, such as in secretory cell lineages or in senescence.

Regardless of how general this response is, our data clearly show that PSRs are key for efficient cytokine responses. In the context of cancer, the downregulation of P-stalk proteins or the inhibition of the PSR could plausibly be a mechanism through which tumor cells avoid immunosurveillance or resist immunotherapy. We have shown that P-stalk mRNA correlates with IFNγ and $CD8^+$ T cell signatures; however, these data are from bulk RNA sequencing (RNA-seq), and testing causation in such data is impossible. Indeed, the signature may be caused by high P-stalk levels in other contributing cell types, although most cells already express them at extremely high levels. Additionally, as expression levels are not necessarily indicative of P-stalk incorporation into the ribosome, this is likely to be a sub-optimal measure of PSR abundance. Regardless, we believe that the findings we have described here show that further analysis of patient data is warranted.

To summarize, we have identified a novel master regulator of cytokine responses that acts at the level of translational control of gene expression. While the technologies to study specialized ribosomes in patient tissue in a high-throughput manner are currently lacking, it will be an important feature to consider in future studies and may present therapeutic applications.

Limitations of the study

There are significant limitations inherent to working with the ribosome. In particular, due to its highly structured nature, tagging RPs runs the risk of altering that structure and potentially interfering with its function. This needs to be considered in the context of the ribosome profiling presented here, although the use of good controls and orthogonal techniques gives us a high level of confidence in our results. Alongside this, KD experiments also face similar risks by potentially reducing the number of competent ribosomes. Differentiating between phenotypes driven by specialized ribosomes and those driven by changes in the concentration of functional ribosomes can be difficult and is something we have tackled by using multiple orthogonal approaches.

Resource availability

Lead contact

Further information and requests for resources and reagents should be directed to and will be fulfilled by the lead contact, William James Faller (w.faller@nki.nl).

Materials availability

All materials used in this study are specified in the key resources table and STAR Methods. All unique reagents generated in this study are available from the lead contact without restriction.

Data and code availability

•The proteomics data have been deposited and are publicly available at the PRIDE repository under accession number PRIDE: PXD041688.

•The Ribo-seq data have been deposited and are publicly available at Gene Expression Omnibus (GEO) with the ID GEO: GSE230060.

•Any additional information required to reanalyze the data reported in this work paper is available from the lead contact upon request.

Acknowledgments

A.D. and S.R. are supported by the NWO (OCENW-M20-373). A.D. is supported by the Mark Foundation (21-053-ASP). F.A., J.S., and Y.M. are supported by the KWF (13878). R.B. and E.M. are supported by the KWF (12539).

Author contributions

A.D., P.K., and W.J.F. designed and conceived the study. Data were generated and analyzed by A.D., F.A., Y.M., K.H., M.K., A.G., J.S., S.R., L.H., and R.v.d.K. Computational analyses were carried out by F.A. and O.I.I. Manuscript was written and edited by A.D., J.W.Y., P.K., and W.J.F. All authors provided feedback on the analyses and edited and approved the manuscript.

Declaration of interests

The authors declare no competing interests.

Methods

Key recources table

REAGENT or RESOURCE	SOURCE	IDENTIFIER
Antibodies		
Hamster anti-mouse TCRβ (clone H57-597)	BD Biosciences	Cat#553172; RRID: AB_394684
Mouse anti-human CD3 (clone OKT3)	BioLegend	Cat#317326; RRID: AB_11150592
Mouse anti-human HLA-A, B, C (clone W6/32)	BioLegend	Cat#311432; RRID: AB_2566151
Mouse anti-human HLA-A2 (clone BB7.2)	BioLegend	Cat#343308; RRID: AB_2561567
Mouse anti-human CD107a (clone H4A3)	BD Biosciences	Cat# 561340; RRID: AB_10642585
Mouse anti-human CD8 (clone SK1)	BD Biosciences	Cat#612889; RRID: AB_2833078
Mouse anti-human IFNγ (clone B27)	BD Biosciences	Cat#554702; RRID: AB_398580
Mouse anti-human TNFα (clone Mab11)	BD Biosciences	Cat#554512; RRID: AB_395443
Mouse anti-human CD80 (clone 2D10)	BioLegend	Cat#305217; RRID: AB_1877254
Rat anti-human HLA-B (clone YTH/76.3)	BD Biosciences	Cat#752625; RRID: AB_2917611
Mouse anti-human HLA-C (clone DT-9)	BioLegend	Cat#373307; RRID: AB_2894582
Mouse anti-human β2-microglobulin (clone A17082A)	BioLegend	Cat#395711; RRID: AB_2801060
Mouse anti-mouse H-2Kb (clone AF6-88.5)	BD Biosciences	Cat#742860; RRID: AB_2741102
Mouse anti-mouse H-2Db (clone KH95)	BD Biosciences	Cat#562000; RRID: AB_11153687
Mouse anti-mouse β2-microglobulin (clone S19.8)	BD Biosciences	Cat#749215; RRID: AB_2873593

Rat anti-mouse H-2 Class I (clone M1/42)	BD Biosciences	Cat#749709; RRID: AB_2873963
Rat anti-mouse CD45 (clone 30-F11)	BioLegend	Cat#103128; RRID: AB_493715
Rat anti-mouse CD11b (clone M1/70)	BD Biosciences	Cat#562605; RRID: AB_11152949
Rat anti-mouse Ly-6G/Ly-6C (Gr-1) (clone RB6-8C5)	BioLegend	Cat#108412; RRID: AB_313377
Rat anti-mouse F4/80 (clone BM8)	BioLegend	Cat#123114; RRID: AB_893478
Mouse anti-mouse CD11c (clone N418)	Thermo Fisher	Cat#35-0114-82; RRID: AB_469709
Rat anti-mouse I-A/I-E (MHCII) (clone M5/114/15.2)	BD Biosciences	Cat#563415; RRID: AB_2738192
Mouse anti α-Tubulin (DM1A)	Cell Signaling Technology	Cat#3873; RRID: AB_1904178
Mouse anti-HSP 90α/β	Santa Cruz Animal Health	Cat#sc-13119; RRID: AB_675659
Rabbit anti-RPL28	Abcam	Cat#ab138125
Mouse anti-human RPLP1	LifeSpan Biosciences	Cat#LS-C198116-100
Rabbit anti-mouse RPLP1	Abbexa	Cat# abx005158
Rabbit anti-RPLP2	Abcam	Cat#ab154958
Rabbit anti-RPS10	Thermo Fisher	Cat# PA5-21390; RRID: AB_11155585
Rabbit anti-RPS28	Thermo Fisher	Cat# PA5-45721; RRID: AB_2608349
Rabbit anti-RPL7	Thermo Fisher	Cat#PA5-36571; RRID: AB_2553591
Rabbit anti-RPL22	Novus Biologicals	Cat#NBP1-98446; RRID: AB_3244375
Mouse anti-HLA Class 1 ABC	Abcam	Cat#ab70328; RRID: AB_1269092
Mouse anti-MART-1/Melan-A	Thermo Fisher	Cat#MS-716-P; RRID: AB_141876
Rabbit anti-NY-ESO-1	Thermo Fisher	Cat#PA5-116201; RRID: AB_2900835

Rabbit anti-Phospho-eIF2α (Ser51)	Cell Signaling Technology	Cat#9721; RRID: AB_330951
Mouse anti-Stat1 (9H2)	Cell Signaling Technology	Cat#9176; RRID: AB_2240087
Rabbit anti-phospho Stat1 (Tyr701)	Cell Signaling Technology	Cat#9167; RRID: AB_561284
HA-Tag	Cell Signaling Technology	Cat#3724; RRID: AB_1549585
IRDye® 800CW Goat anti-Rabbit IgG	LI-COR	Cat#926-32211; RRID: AB_621843
IRDye® 680RD Goat anti-Mouse IgG	LI-COR	Cat# 926-68070; RRID: AB_10956588
Chemicals, peptides, and recombinant proteins		
Recombinant human IFNγ	Peprotech	Cat#300-02
Recombinant human TNFα	Peprotech	Cat#300-01A
Recombinant human IFNα	Peprotech	Cat#
Recombinant human IFNβ	Peprotech	Cat#300-02BC
Recombinant human TGFβ1	Peprotech	Cat#100-21
Recombinant human IL-1β	Peprotech	Cat#200-01B
Recombinant human IL-6	Peprotech	Cat#200-06
Recombinant human IL-7	ImmunoTools	Cat#11340073
Recombinant human IL-15	ImmunoTools	Cat#11340153
Recombinant human IL-17A	Peprotech	Cat#200-17
Recombinant human M-CSF	Peprotech	Cat#300-25
Recombinant mouse M-CSF	BioLegend	Cat#576408
Recombinant mouse GM-CSF	Peprotech	Cat#315-03
Prostaglandin E_1	Sigma-Aldrich	Cat#P5515
Lipopolysaccharides from *Escherichia coli* (LPS)	Sigma-Aldrich	Cat#L4391
Incucyte Caspase-3/7 Green Dye	Satorius	Cat#4440
^{35}S-methionine label	Hartmann Analytic	Cat#ARS0110
SYBR™ Green PCR Master Mix	Thermo Fisher	Cat# 4367659
Cycloheximide	Sigma-Aldrich	Cat#C7698
Critical commercial assays		
Miltenyi CD8+ T Cell Isolation Kit, human	Miltenyi Biotec	Cat#130-096-495
Miltenyi CD14 MicroBeads, human	Miltenyi Biotec	Cat#130-050-201
Dynabeads Human T-Activator CD3/CD28	Miltenyi Biotec	Cat#111.31D
Deposited data		

Proteomics data	This paper	PRIDE: PXD041688
RiboSeq data	This paper	GEO: GSE230060
Experimental models: Cell lines		
Human: Mel624 cell line	Patel et al.[33]	N/A
Human: M026 cell line	Patient-derived	N/A
Human: T cells transduced with HLA-A2-recognizing melanoma antigen MART-1	Patient-derived	N/A
Human: T cells transduced with HLA-A2-recognizing melanoma antigen NY-ESO-1	Patient-derived, Patel et al.[33]	N/A
Human: HEK293T	Sigma-Aldrich	Cat#12022001
Mouse: B16-F10 cell line	ATCC	Cat#CRL-6475
Oligonucleotides		
shRNA targeting sequence: Ctrl#1: CCTAAGGTTAAGTCGCCCTCG	This paper	N/A
shRNA targeting sequence: Ctrl#2: CAACAAGATGAAGAGCACCAA	This paper	N/A
shRNA targeting sequence: eL28: CCGCAATTCCTTCCGCTACAA	Wei et al.[29]	N/A
shRNA targeting sequence: P1#1 GTCACGGAGGATAAGATCAAT	This paper	N/A
shRNA targeting sequence: P1#3 CGTCAACATTGGGAGCCTCAT	This paper	N/A
shRNA targeting sequence: eL6 GTATTCCCGATCTGCCATGTA	This paper	N/A
shRNA targeting sequence: uL30 GCGAATTGCTTTGACAGATAA	Wei et al.[29]	N/A
shRNA targeting sequence: eS10 GTATCCAGTATCTCCGTGATT	Wei et al.[29]	N/A
shRNA targeting sequence: eS28 CGATCCATCATCCGCAATGTA	Wei et al.[29]	N/A
crRNA targeting sequence: *RPLP2* GAAGAGTCAGATGATGACAT	This paper	N/A
ssODN *RPLP2* phospho-dead (S102A TCT>gCT, S105A TCA>gCA) sequence: TTCCACAGCAGAGGAGAAGAAA GATGAGAAGAAGGAGGAGgCTGAAGAagCAGATGAT G AtATGGGATTTGGCCTTTTTGATTAAATTCCTGCTCC CCT	This paper	N/A
ssODN *RPLP2* phospho-mimicking (S102D TCT>gaT, S105D TCA>gac) sequence: TTCCACAGCAGAGGAGAAGAAAGAT GAGAAGAAGGAGGAGgaTGAAGAagacGATGATGAtA TGGG ATTTGGCCTTTTTGATTAAATTCCTGCTCCCCT	This paper	N/A
Primer: *RPLP2* (phospho) forward: AGGCAAGTCCCTGGATA GGA, reverse: GCCCTGATTACCCAAACTCCA	This paper	N/A

Primer: *RPLP2* sequencing forward: GAAGTCCCCGTTGAGG AGTG	N/A	N/A
Primer: *ACTB* forward: CCTGGCACCCAGCACAAT, reverse: GGGCCGGACTCGTCATACT	This paper	N/A
Primer: *RPL28* forward: GTGCCTCAGTTTCCCATATGTA, reverse: TACTGGACTAAGAGCTGGAGAG	This paper	N/A
Primer: *RPLP1* forward: CCTATACAACCCTGCCTAAGAAC, reverse: CCCAAACATTTGGTGAGACATTAC	This paper	N/A
Primer: *RPLP2* forward: ACCGGCTCAACAAGGTTATC, reverse: CAGCAGGTACACTGGCAA	This paper	N/A
Primer: *HLA-A* forward: AAGAGTTGTTCCTGCCCTTC, reverse: CCTCCTCACATTATGCCTACAC	This paper	N/A
Primer: *HLA-B* forward: GACACTGAGCTTGTGGAGAC, reverse: GGCATGTGTATCTCTGCTCTT	This paper	N/A
Primer: *HLA-C* forward: AATGTGAGGAGGTGGAGAGA, reverse: CCTCTCTGGAACAGGAAAGATG	This paper	N/A
Recombinant DNA		
pLV[shRNA]-mCherry:T2A:Puro-U6>	Vectorbuilder	N/A
DECIPHER pRSI9-U6- (sh)-UbiC-TagRFP-2A-Puro	Wei et al.[29]	Addgene Plasmid #28289; RRID: Addgene_28289
pMDLg/pRRE	Dull et al.[64]	Addgene Plasmid #12251; RRID: Addgene_12251
psPAX2	The Trono Laboratory	Addgene Plasmid #12260; RRID: Addgene_12260
pVSV-G	Gee et al.[65]	Addgene Plasmid #138479; RRID: Addgene_138479
pRSV-REV	Dull et al.[64]	Addgene Plasmid #12253; RRID: Addgene_12253
Software and algorithms		
FlowJo version 10.8.1	FlowJo LLC	N/A
Incucyte Base Analysis Software	Satorius	N/A
ImageStudioLite Software version 5.2.5	LI-COR	N/A
Empiria Studio Software version 1.3.0.83	LI-COR	N/A

MaxQuant version 1.6.15.0	Tyanova et al.[66]	N/A
DIA-NN (version 1.8)	Demichev et al.[67]	N/A
DESEQ2	Love et al.[68]	N/A
clusterProfiler package	Yu et al.[69]	N/A
Deposited data		
Proteomics	PRIDE	PXD041688
Ribosome profiling	Gene Expression Omnibus (GEO)	GSE230060

Experimental model and study participant details

Cell culture

M026, Mel624, mouse B16, hTERT-RPE1, SK-OV-3 and HCT 116 cells were maintained in DMEM supplemented with 10% FBS and 100 U/ml Penicillin- 100ug/ml Streptomycin (Life Technologies 15140-122). HEK293T cells were maintained in Iscove's Modified Dulbecco's Medium (IMDM) supplemented with 10% FCS and 100 U/ml Penicillin- 100ug/ml Streptomycin.

Patient material

Human peripheral blood mononuclear cells (PBMCs) were derived from buffy coats of donors at the Netherlands Cancer Institute (Amsterdam, The Netherlands). PBMC isolation was performed using a standard Ficoll gradient centrifugation separation. Isolated PBMCs were either processed directly or cryopreserved in liquid nitrogen and fetal bovine serum (FBS) with 10% dimethyl sulfoxide (DMSO).

Animal housing and ethics

Ex vivo harvesting of murine organs was approved by the Animal Ethics Committee of the Netherlands Cancer Institute. Handling and housing of mice was followed according to institutional, national and European guidelines for Animal Care and Use. Murine organs were obtained from wild-type C57BL/6J mice that were 6-12 weeks old (Janvier laboratories). All mice were of female gender to reduce experimental variability.

Primary cells

To generate human monocyte-derived macrophages, $CD14^+$ monocytes were isolated using CD14 Microbeads (Miltenyi Biotec 130-050-201) according to manufacturer's instructions.

$CD14^+$ monocytes were then cultured in macrophage medium (Roswell Park Memorial Institute 1640 Medium (RPMI) 1640 supplemented with 2mM Ultraglutamine I, 100 U/ml Penicillin- 100ug/ml Streptomycin, and 2% human serum (HS, Sigma-Aldrich)) in the presence of 15ng/ml M-CSF (Peprotech 300-25) for macrophage differentiation. Medium and cytokines were refreshed every 2-3 days. Macrophages were activated 24h prior to the experiment using 10ng/ml IFNγ (Peprotech 300-02) and 50ng/ml LPS (Sigma-Aldrich L4391). Macrophage activation was confirmed by flow cytometry using CD80 expression (clone 2D10, Biolegend 305217).

To generate murine bone marrow-derived dendritic cells (BMDCs) and macrophages (BMDMs), murine bone marrow cells were obtained from the tibia and femurs of wild-type C57BL/6J mice as previously described [79]. Briefly, murine bones were flushed with Dulbecco's Modified Eagle Medium (DMEM) supplemented with 10% FBS using a 23G needle. The resulting cell suspension was filtered with a 100µm cell strainer and resuspended in 40mL DMEM containing 10% FBS. The cell suspension was divided in half (20mL each) and cultured for 5 days in 2 separate 40mL PermaLife™ cell culture bags (OriGen, product code PL30-2G) supplemented with either 10ng/ml recombinant mouse M-CSF (BioLegend 576408) to generate BMDMs or 20ng/ml recombinant mouse GM-CSF (Peprotech 315-03) to generate BMDCs, respectively. Culture medium and cytokines were refreshed every 2 days. Five days after differentiation, BMDCs and BMDMs were harvested from the bags and centrifuged for 5 minutes at 300 x g and used for *in vitro* experiments. BMDCs were matured 24h prior to the experiment using 10ng/ml TNFα (Peprotech 300-01A), 10ng/ml IL-6 (Peprotech 200-06), 10ng/ml IL-1β (Peprotech 200-01B) and 0.5µg/ml PGE-1 (Sigma-Aldrich P5515).

Generation of MART-1 and NY-ESO-1 TCR CD8 T cells

TCR transduced $CD8^+$ T cells were isolated from PBMCs as described previously [70]. After PBMC isolation, $CD8^+$T cells were isolated with the Miltenyi $CD8^+$ T Cell Isolation Kit, human (Miltenyi Biotec 130-096-495) and stimulated with Dynabeads Human T-Activator CD3/CD28 (Miltenyi Biotec 111.31D) for 48 hours at 37°C. Activated $CD8^+$T cells were mixed with MART-1 or NY-ESO-1 TCR containing retrovirus, added on a retronectin-coated (Takara T100A) non-tissue culture 24-well plate and spun for 90 minutes at 2500 rpm at 10°C. Subsequently, TCR-transduced $CD8^+$ T cells were harvested and maintained in T cell medium containing RPMI supplemented with 100 U/ml Penicillin- 100ug/ml Streptomycin and 10% human serum (Sigma-Aldrich), IL-7 (ImmunoTools 11340073, 5ng/ml), IL-15 (ImmunoTools 11340153, 5ng/ml). After 7 days, TCR transduction efficiency was measured by flow cytometry using the PE a-mouse TCRβ antibody (clone H57-597, BD Biosciences 553172) and anti-PE

MicroBeads (Miltenyi Biotec 130-048-801). Finally, TCR-transduced $CD8^+$ T cells were rapidly expanded for 5 days using irradiated feeder PBMCs and medium containing 60U/ml IL-2 (Proleukin, Novartis) and Ultra-LEAF™ Purified anti-human CD3 Antibody (clone OKT3, BioLegend 317326, 1:2000). After 5 days, T cells were expanded for additional 2 weeks in medium without the Ultra-LEAF™ Purified anti-human CD3 Antibody and stored at -80°C until needed.

Generation of RPLP2 phospho-dead and mimicking cell lines

To generate a RPLP2 phospho-dead and mimicking cell line, we made use of the IDT Alt CRISPR-Cas9 System (IDT). The endogenous RPLP2 locus was targeted using a sgRNA composed of crRNA (IDT, GAAGAGTCAGATGATGACAT) fused to Alt-R CRISPR-Cas9 tracrRNA, ATTO™ 550 (IDT 1075828) in a final concentration of 50μ M. 0,2x10ˆ6 cells per condition were resuspended in 20μ l SE Cell Line Nucleofection Solution (Lonza V4XC-1024) and mixed with RNP complexes consisting of 50μ M RPLP2-targeting sgRNA, 62μ M Alt-R™ S.p. Cas9 Nuclease V3 (IDT 1081058) and a 50μ M ssODN sequence to generate RPLP2 phospho-dead (S102A TCT>gCT, S105A TCA>gCA; 5' - TTCCACAGCAGAGGAGAAGAAAGATGAGAAGAAGGAGGAGgCTGAAGAagCAGATGAT GAtATGGGATTTGGCCTTTTTGATTAAATTCCTGCTCCCCT - 3') or RPLP2 phospho-mimicking (S102D TCT>gaT, S105D TCA>gac; 5'- TTCCACAGCAGAGGAGAAGAAAGATGAGAAGAAGGAGGAGgaTGAAGAagacGATGATG AtATGGGATTTGGCCTTTTTGATTAAATTCCTGCTCCCCT -3') cells. The cell-RNP solution was incubated for 20 minutes at room temperature and transferred to a nucleocuvette and electroporated using the standard program CA-137 following the Lonza Amaxa 4D-Nucleofector Protocol (Lonza AAF-1003X). Pre-warmed culture medium was added to each cuvette, resuspended and nucleofected cells were divided into 2 wells of a 24-well plate. Cells were incubated at 37°C and ultimately, serial dilutions (1 cell/well) were plated in 5x96 well plates. Single cell-derived clones were harvested and expanded, and genomic DNA was isolated using the ISOLATEII genomic DNA kit (Bioline BIO-52066). To assess editing efficiency, gDNA was extracted and amplified by PCR using the following primers: *RPLP2* forward (5'-AGGCAAGTCCCTGGATAGGA-3') and *RPLP2* reverse (5'-GCCCTGATTACCCAAACTCCA-3'). PCR products were purified using the QIAquick PCR purification Kit (QIAGEN 28104) and sequenced using eurofins genomic services to assess editing efficiency using a RPLP2 sequencing primer (5'- GAAGTCCCCGTTGAGGAGTG -3'). This resulted in a 100% editing efficiency for both RPLP2 phospho-dead cell clones (clone#23 and #24), which were used for the experiments described in this paper. For RPLP2 phospho-mimicking cells this resulted in an editing efficiency of 94% and 82%, respectively (clone#9

and #11). However, RPLP2 phospho-mimicking cells were not viable and could not be used in experiments.

Cytokine treatment

Cytokine stimulation was performed using the following cytokines: human recombinant IFNγ (Peprotech 300-02, 50ng/ml) and human recombinant TNFα (Peprotech 300-01A, 50ng/ml), human recombinant IFNα (Immunotools 11343516, 10ng/ml) and human recombinant IFN β (Peprotech 300-02BC, 10ng/ml), human recombinant TGFβ (Peprotech 100-21, 2ng/ml), human recombinant IL-6 (Peprotech 200-06, 10ng/ml), human recombinant IL-1β (Peprotech 200-01B, 10ng/ml) or human recombinant IL-17A (Peprotech, 200-17, 100ng/ml). Initially, cytokines were reconstituted in PBS containing 0.1% bovine serum albumin (BSA). Cells were treated for 24h or 48h unless stated otherwise.

Lentivirus shRNAs

All shRNA targeting sequences were cloned into a pLV[shRNA]-mCherry:T2A:Puro-U6> vector purchased from Vectorbuilder or into DECIPHER pRSI9-U6- (sh)-UbiC-TagRFP-2A-Puro [29]. shRNA targeting sequences were selected based on previous literature [29] and the RNAi consortium at the Broad Institute (https://portals.broadinstitute.org/gpp/public/). The shRNA target sequences used in this paper were: CCTAAGGTTAAGTCGCCCTCG (shCtrl#1), CAACAAGATGAAGAGCACCAA (shCtrl#2), CCGCAATTCCTTCCGCTACAA (shL28), GTCACGGAGGATAAGATCAAT (shP1#1), CGTCAACATTGGGAGCCTCAT (shP1#3), GTATTCCCGATCTGCCATGTA (shL6), GCGAATTGCTTTGACAGATAA (shL30), GTATCCAGTATCTCCGTGATT (shS10) and CGATCCATCATCCGCAATGTA (shS28). HEK293T (Sigma-Aldrich, 12022001) cells were used for lentiviral packaging using a second (pMDL RRE and psPAX2) or third-generation (pVSV-G, pRSV-REV and pMDLg/RRE) packaging system. Tumor cells, BMDMs and BMDCs were infected with shRNA lentivirus containing supernatant at a MOI=0.5 and transduction efficiency of tumor cell lines was measured by flow cytometry 96 hours or 7 days after infection, respectively. This resulted in a transduction efficiency of 80-100% of target cells determined by mCherry (%) expression. Human primary macrophages were transduced with 100x concentrated lentivirus, generated using Lenti-X™ Concentrator (Takara 631232) according to manufacturer's instructions, and 5μg/ml polybrene (Sigma-Aldrich). After incubation for 6 hours at 37°C, fresh culture medium containing M-CSF was added to the well. On the next day, medium was refreshed with culture medium containing 15ng/ml M-CSF and every other day after that.

HLA class I surface staining

To assess HLA class I surface expression, tumor cells were stained for 30 minutes with BV605™ anti human HLA-A, B, C (clone W6/32, BioLegend 311432), APC anti human HLA-A2 (clone BB7.2, BioLegend 343308), BUV805 anti human HLA-B (clone YTH/76.3, BD Biosciences 752625), AF647 anti human HLA-C (clone DT-9, Biolegend 373307), APC anti human β2-microglobulin (clone A17082A, Biolegend 395711), BV605 anti mouse H-2Kb (clone AF6-88.5, BD Biosciences 742860), FITC anti mouse H-2Db (clone KH95, BD Biosciences 562000), BUV805 anti mouse β2-microglobulin (clone S19.8, BD Biosciences 749215), BUV605 anti mouse H-2 class I (clone M1/42, BD Biosciences 749709). HLA I levels in mouse BMDMs were measured using anti-mouse H-2 class I and anti-mouse β2-microglobulin antibodies, gated on $CD45^+$ (clone 30-F11, Biolegend 103128) / $CD11b^+$ (clone M1/70, BD Biosciences 562605) / $GR\text{-}1^-$ (clone RB6-8C5, Biolegend 108412) / $F4/80^+$ (clone BM8, Biolegend 123114) cells. BMDCs were gated on $CD45^+$ / $CD11b^+$ / $GR\text{-}1^-$ / $F4/80^-$ / $CD11c^+$ (clone N418, Invitrogen 35-0114-82) / $MHCII^+$(clone M5/114/15.2, BD Biosciences 563415) cells. Cell viability was measured using the LIVE/DEAD Fixable IR Dead Cell Stain Kit (Thermo Fisher L10199). Flow cytometric data were acquired using the BD FACSymphony™ flow cytometer (BD Biosciences), gated on single and live cells. Data were analyzed with the FlowJo version 10.8.1 software (FlowJo LLC).

HLA class I peptide complex recovery

Tumor cells were washed with PBS and treated for 2 minutes with ice cold citric acid buffer (0.13M citric acid, 0.061 M Na2HPO4, 0.15 M NaCl at pH 3). Cells were washed three times with ice cold PBS, resuspended in culture medium and kept at 37°C. At indicated time points, cells were stained with HLA-A, B, C (clone W6/32, BioLegend 311432) and APC anti HLA-A2 (clone BB7.2, BioLegend 343308) and HLA surface levels were measured on the BD FACSymphony™ flow cytometer (BD Biosciences) using the MFI.

Co culture experiments

MART-1 or NY-ESO-1 specific $CD8^+$ T cells were thawed one day prior to the experiment in RPMI containing Penicillin - Streptomycin, 10% HS and DNase I (Sigma-Aldrich 10104159001, 1/1000) for 30 minutes. Cells were recovered overnight in RPMI supplemented with Penicillin - Streptomycin, 10% HS, IL-7 (5ng/ml) and IL-15 (5ng/ml). T cells and RP KD tumor cells were then co-cultured for 6 hours in the presence of GolgiPlug (BD Biosciences 555029) and GolgiStop (BD Biosciences 554724) at a T cell:target ratio of 1:1. After 6 hours, cells were stained with AF700 anti CD107a (clone H4A3, BD Biosciences 561340), BUV anti CD8 (clone SK1, BD Biosciences 612889) and the LIVE/DEAD Fixable IR Dead Cell Stain Kit.

Subsequently, cells were fixed and permeabilized with the Foxp3 Transcription Factor Staining Buffer Set (eBioscience, 00-5523-00). Intracellular cytokine staining was performed using APC anti IFNγ (clone B27, BD Biosciences 554702) and FITC anti TNFα (clone MAb11, BD Biosciences 554512). Fixed cells were measured the following day using the BD FACSymphony™ flow cytometer (BD Biosciences), gated on single, live $CD8^+$ T cells. Data were analyzed with the FlowJo version 10.8.1 software (FlowJo LLC).

Incucyte killing assay

MART-1 or NY-ESO-1 specific $CD8^+$ T cells were thawed one day prior to the experiment as described above. To measure tumor cell death, tumor cells were stained with the Incucyte Caspase-3/7 Green Dye (Satorius 4440, 5µM). Subsequently, MART-1 or NY-ESO-1 specific $CD8^+$ T cells were added at a T cell:target ratio of 1:1. As a negative control, tumor cells were cultured without T cells. After allowing cells to settle for 30 minutes, live-cell fluorescent images were captured every 2 hours with the Incucyte Live-Cell Analysis System (Satorius) for 48 hours in total. Of note, shL28 tumor cells were hypersensitive to cell contact induced apoptosis, which resulted in increased tumor death after 24h in both cell lines expressing shL28. Therefore, these lines were analyzed only until the 24h time point. T cell killing was assessed with the integrated Incucyte Base Analysis Software (Satorius) using dead tumor cell count. Importantly, each data timepoint was analyzed to the negative control to account for tumor death without T cells.

^{35}S-methionine incorporation assay

Assessment of protein synthesis using ^{35}S-methionine labelling was performed as described previously [71]. In short, tumor cells were labelled with 30 µCi/ml ^{35}S-methionine label (Hartmann Analytic ARS0110) for 2 hours at 37°C. After washing cells with PBS, cells were lysed with lysis buffer (50 mM TrisHCl pH 7.5, 150 mM NaCl, 1% Tween-20, 0.5% NP-40, protease inhibitor cocktail (Roche 5892791001) and phosphatase inhibitor cocktail (Sigma P5726). Protein was precipitated onto Whatmann filter paper using 25% trichloroacetic acid (TCA). After washing with 70% ethanol and acetone, scintillation was measured with the liquid scintillation counter (Perkin Elmer). For data analysis, radioactive counts were normalized to total protein amounts.

Immunoblotting

Tumor cells were washed in PBS and pellets were lysed for 20 minutes on ice in lysis buffer (100mM Hepes pH 7.5, 300mM NaCl, 10mM EGTA, 3mM $MgCl_2$, 2% glycerol, 2% triton X-100 (Sigma), protease inhibitor cocktail (Roche 5892791001) and phosphatase inhibitor

cocktail (Sigma P5726). Protein amounts were quantified with the Pierce™ BCA Protein Assay Kit (Thermo Scientific 23227) and equal protein amounts were separated using ready-to-use 4–20% Mini-PROTEAN® TGX Stain-Free™ Protein Gels (Biorad, 4568096) and transferred onto 0.2 µm pore nitrocellulose membranes (PALL Life Sciences 66485). Subsequently, dry membranes were blocked for 1 hour at room temperature using Intercept (TBS) Blocking Buffer (LI-COR, 927-66003). After blocking, membranes were incubated with primary antibodies overnight at 4°C followed by incubation with secondary antibodies IRDye® 800CW Goat anti-Rabbit IgG (LI-COR 926-32211, 1: 10000) and IRDye® 680RD Goat anti-Mouse IgG (LI-COR, 926-68070, 1:10000) for 1 hour at room temperature. Data were acquired with the Odyssey CLx (LI-COR) and analysed using the software ImageStudioLite version 5.2.5 (LI-COR) or Empiria Studio version 1.3.0.83 (LI-COR). Primary antibodies used were: α-Tubulin (DM1A, Cell Signaling Technology 3873, 1:1000), HSP 90α/β (Santa Cruz Animal Health sc-13119, 1:1000), RPL28 (Abcam ab138125, 1:1000), RPLP1 (LifeSpan Biosciences LS-C198116-100, 1:1000), RPLP2 (Abcam ab154958, 1:1000), HLA Class 1 ABC (Abcam, ab70328, 1:1000), MART-1/Melan-A (Thermo Fisher MS-716-P, 1:1000), NY-ESO-1 (Thermo Scientific PA5-116201, 1:500), Phospho-eIF2α (Ser51) (Cell Signaling Technology 9721, 1:1000), RPL7 (Thermo Scientific PA5-36571, 1:1000), RPL22 (Novus Biologicals NBP1-98446, 1:1000), HA-Tag (Cell Signaling Technology 3724, 1:1000), anti-mouse RPLP1 (Abbexa abx005158, 1:500), RPS10 (Thermo Scientific PA5-21390), RPS28 (Thermo Scientific PA5-45721), Stat1 (Cell Signaling Technology 9176) and phospho-Stat1 (Cell Signaling Technology 9167).

RNA isolation and RT-qPCR

RNA was isolated with the ISOLATE II RNA Mini Kit (BioCat BIO-52072-BL) according to the manufacturer's protocol. Isolated RNA was resuspended in nuclease-free water and quantified using the Nanodrop (Thermo Scientific). Subsequently, High-Capacity cDNA Reverse Transcription Kit (Thermo Scientific 4368814) was used for reverse transcription and SYBR™ Green PCR Master Mix (Thermo Fisher 4367659) was used for qPCR. Gene expression levels were analysed in three technical replicates by using the comparative CT method and data were normalised to the housekeeping gene *ACTB*. The used primer sequences for qPCR were: *ACTB* forward (5'-CCTGGCACCCAGCACAAT-3'), *ACTB* reverse (5'-GGGCCGGACTCGTCATACT-3'), *RPL28* forward (5'- GTGCCTCAGTTTCCCATATGTA-3'), *RPL28* reverse (5'-TACTGGACTAAGAGCTGGAGAG-3'), *RPLP1* forward (5'-CCTATACAACCCTGCCTAAGAAC-3'), *RPLP1* reverse (5'-CCCAAACATTTGGTGAGACATTAC-3'), *RPLP2* forward (5'-ACCGGCTCAACAAGGTTATC-3'), *RPLP2* reverse (5'-CAGCAGGTACACTGGCAA-3'), *HLA-A* forward (5'-AAGAGTTGTTCCTGCCCTTC-3'), *HLA-A* reverse (5'-

CCTCCTCACATTATGCCTACAC-3'), *HLA-B* forward (5'-GACACTGAGCTTGTGGAGAC-3'), *HLA-B* reverse (5'-GGCATGTGTATCTCTGCTCTT-3'), *HLA-C* forward (5'-AATGTGAGGAGGTGGAGAGA-3'), *HLA-C* reverse (5'-CCTCTCTGGAACAGGAAAGATG-3').

Polysome fractionation (protein precipitation and RNA extraction)

Tumor cells were lysed in ice cold polysome lysis buffer (10x gradient buffer (1.1M potassium acetate, 0.2M magnesium acetate, 0.1M HEPES pH 7.6), 100mM KCl, 10mM $MgCl_2$, 0.1% NP-40, 154.25mg/ml DTT, 100 µg/ml cycloheximide (Sigma-Aldrich C7698), RNaseOUT™ Recombinant Ribonuclease Inhibitor (Thermo Scientific 10777019) and combined Halt™ Protease and Phosphatase Inhibitor EDTA-free (Thermo Scientific 78443)). Lysates were passed through a needle (27G) and cleared by centrifugation at 14.000 x g for 10 minutes. Subsequently, 50ul of cleared supernatant was collected to measure the total protein or RNA amount while the rest was loaded onto a 10%-60% sucrose gradient and centrifuged under vacuum at 38.000 rpm for 2 hours at 4°C. Subsequently, monosome-containing fractions 6-8 (750ul per fraction) and polysome-containing fractions 9-14 (750ul per fraction) were collected and protein was extracted using a standard TCA precipitation protocol [72].

For RNA extraction from sucrose gradients, each fraction (fraction 1-14) was collected separately and incubated with 20mg/ml Proteinase K (Thermo Scientific 25530049, 1:100), 0.5M EDTA and 20% SDS for 30 minutes at 42°C. Afterwards, samples were mixed with phenol:chloroform and centrifuged for 8 minutes at 14.000 x g. Subsequently, RNA was extracted with 100% EtOH and sodium acetate and centrifuged for 30 minutes at 14.000 x g. Samples were then washed with 80% EtOH and centrifuged for 10 minutes at 14.000 x g. Finally, RNA pellets were reconstituted in nuclease-free water, incubated for 5 minutes at 60°C and stored at -80°C.

Protein quantification with LC-MS

Quantification of ribosomal fractions

Dry protein pellets were dissolved in 100mM TrisHCL (pH 8.5, Sigma T1503) to determine the protein concentration using the Bradford protein assay (Thermo Scientific 23200). Subsequently, proteins were reduced and alkylated with dithiothreitol (Sigma 43815) and iodoacetamide (Sigma I6125) and digested twice with trypsin (Promega VA9000) at 37°C. The digests were dried, reconstructed with 5% formic acid (Honeywell|FlukaTM 94318) and desalted with C18 StageTips (Thermo Scientific 87781). Before proceeding with mass spectrometry, the digests were reconstructed with 2% formic acid. All samples were analyzed

using a nanoLC-MS/MS system consisting of an Orbitrap Exploris 480 mass spectrometer coupled to an EASY-NLC 1200 system (Thermo Scientific). The proteins were separated on an analytical column (ReproSil-Pur 120 C18-AQ, 2.4 µm, 75 µm × 500 mm, packed in-house) using a linear gradient of solvent A (0.1% formic acid/water, Fischer Chemical LS122) and solvent B (0.1% formic acid/80% acetonitrile, Fischer Chemical LS118), with a flow rate of 250 nl/minutes in a 90-minutes gradient. The gradient contained a 70-minutes linear increase from 6% to 30% solvent B, followed by a 20-minutes wash at 90% solvent B.

Total protein quantification

For protein digestion, frozen cell pellets were lysed in boiling Guanidine (GuHCl) lysis buffer as described by Jersie-Christensen et al [73]. Protein concentration was determined with a Pierce Coomassie (Bradford) Protein Assay Kit (Thermo Scientific), according to the manufacturer's instructions. After dilution to 2M GuHCl, aliquots of protein were digested twice (overnight and 4h) with trypsin (Sigma-Aldrich) at 37°C, enzyme/substrate ratio 1:75. Digestion was quenched by the addition of FA (final concentration 1%), after which the peptides were loaded on the Evotip Pure™ (Evosep). LC-MS/MS analysis was carried out using an Evosep One LC system connected to an Orbitrap Exploris 480 Mass Spectrometer (Thermo Fisher Scientific). Peptides were separated using the pre-programmed gradient (Extended method, 88 min gradient) on an EV1137 (Evosep) column with an EV1086 (Evosep) emitter. The Exploris 480 was run in data-independent acquisition (DIA) mode, with full MS resolution set to 120,000 at m/z 200, MS1 mass range was set from 350-1400, normalized AGC target was 300% and maximum IT was 45ms. DIA was performed on precursors from 400-1000 in 48 windows of 13.5 Da with an overlap of 1 Da. Resolution was set to 30,000 and normalized CE was 27.

Phosphoproteomics

Phosphopeptide enrichment

Phosphorylated peptides were enriched from 10uG total peptides using a High-Select Fe-NTA Phosphopeptide Enrichment Kit (Thermo Scientific A32992), according to the manufacturer's instructions, with the exception that the resin was split into five aliquots, with each aliquot subsequently loaded onto a StageTip, C8 (Thermo Scientific). Centrifugation steps were performed at 1000 x g for 5 minutes and dried eluates were reconstituted in 15 µL of 2% formic acid.

Quantification of phosphopeptides

Prior to mass spectrometry analysis, the peptides were reconstituted in 2% formic acid. Peptide mixtures were analyzed by nanoLC-MS/MS on an Orbitrap Exploris 480 Mass Spectrometer equipped with an EASY-NLC 1200 system (Thermo Scientific). Samples were directly loaded onto the analytical column (ReproSil-Pur 120 C18-AQ, 2.4 µm, 75 µm × 500 mm, packed in-house). Solvent A was 0.1% formic acid/water and solvent B was 0.1% formic acid/80% acetonitrile. For the phosphoproteome, samples were eluted from the analytical column at a constant flow of 250 nl/min in a 70-min gradient containing a linear increase from 7% to 30% solvent B, followed by a 15-min wash at 90% solvent B.

Sample preparation and HA pulldown

For the HA pulldown, eL22-HA and HA-P1 tumor cells were grown in 4x15cm dishes per condition. Cytokine-treated HA tagged tumor cells were treated with 50ng/ml IFNγ and TNFα for 24 hours. As described previously [71], cells were treated with 200 µg/ml cycloheximide for 3-5 minutes at 37 °C and cell pellets were washed with ice-cold PBS containing 200 µg/ml cycloheximide. Subsequently, pellets were lysed for 30 minutes in ice-cold lysis buffer (20 mM Tris HCl pH 7.4, 10 mM MgCl2, 150 mM KCl, 1% NP-40, 200 µg/mL cycloheximide and 1x EDTA-free proteinase inhibitor cocktail (Sigma 5892791001)). Lysates were centrifuged at 12.000 x g for 20 minutes at 4 °C and the supernatants were collected for RNA digestion using RNaseI (Thermo Scientific AM2294) for 40 minutes at 25 °C. RNA digestion was stopped using SUPERase (Thermo Scientific AM2694). Digested lysates were incubated with Pierce™ Control Agarose Matrix (Thermo Scientific 26150) for 15 minutes at 4°C followed by incubation with AntiHA.11 Epitope Tag Affinity Matrix (BioLegend 900801) for 4 hours at 4°C under constant rotation. Supsequely, tagged ribosomes were eluted with 1mg/ml HA peptide (Thermo Scientific 26184) for 15 minutes at 30°C. Finally, ribosome protected fragments (RPFs) were purified using miRNeasy minikit (Qiagen) according to manufacturer's instructions and RNA concentrations were measured with the Agilent 2100 bioanalyzer using a Small RNA Chip (Agilent 5067-1548).

Ribosome profiling

Ribosome profiling was performed in technical duplicates on purified RPFs of cytokine-treated HA tagged Mel624 tumor cells as described previously [74]. Briefly, RPFs were run on a 15% TBE-urea polyacrylamide gel and size-selected between 26nt and 32nt using RNA markers. RNA was extracted using RNA gel extraction buffer (300 mM NaOAc pH 5.5, 1.0 mM EDTA, 0.25% SDS) and precipitation for 30 minutes on dry ice. After precipitation, samples were incubated overnight at 25°C. End dephosphorylation was performed using T4 polynucleotide

kinase (PNK) (NEB M0201) for 1 hour at 37°C and ligation was performed using the T4 RNA ligase I (NEB M0204) for 2 hours at 25°C. Reverse transcription was performed using the SuperScript III reverse transcriptase (Thermo Scientific 18080051) using the oCJ485 RT primer for 30 minutes at 50°C. cDNA was then size-selected at 110bp using a 10% TBE-urea polyacrylamide gel. DNA was extracted using DNA gel extraction buffer (300 mM NaCl, 10 mM Tris pH 8, 1 mM EDTA) and precipitation for 30 minutes on dry ice. After precipitation, samples were incubated overnight at 25°C. Circular ligation was performed using CircLigase II ssDNA Ligase (Epicentre CL4111K) for 1,5 hours at 60°C. cDNA amplification was performed for 15 cycles with the Phusion High-Fidelty DNA polymerase (Thermo Scienfific F530) and primers containing different indexes for sequencing. The amplification product was size-selected at 180bp using a 8% TBE polyacrylamide gel. Samples were measured with the Agilent 2100 bioanalyzer using a DNA chip (Agilent 5067-1506) to assure high quality followed by molarity quantification. Sequencing was performed on the Illumina HiSeq2500.

Quantification and statistical analysis

Statistical tests and analysis

All statistical test details about each experiment can be found in the figure legends, figures or results, including the statistical test used, exact value of *n* and what *n* represents. All p values are shown for each group and all groups were compared to the untreated or scrambled (shCtrl) control group. Statistical significance between groups was calculated using the tests indicated\ in each figure legend.

Analysis of proteins determined with LC-MS

Raw data were analyzed by DIA-NN (version 1.8) [67] without a spectral library and with “Deep learning” option enabled. The Swissprot human database (20,395 entries, release 2021_04 for ribosomal fractions MS; 20.398 entries, release 2022_08 for P1-KD MS) was added for the library-free search. The Quantification strategy was set to Robust LC (high accuracy) and MBR option was enabled. The other settings were kept at the default values. For ribosomal fractions MS, the protein groups report from DIA-NN was used for downstream analysis in R, whereas, for the P1-KD MS, protein group abundances were extracted from the DIA-NN result files, imported into Perseus (version 2.0.7.0) [66] and were filtered for presence in at least 3 out of 4 replicates in at least one condition. Further analyses were performed in R as follows. For the ribosome-specific analyses of sub-polysome and polysome fractions, samples were first clustered into different fractions and for each independent cluster, RP abundances were normalized using a variance stabilizing normalization (vsn) [75], using solely the abundances of detected RPs. For total protein fraction, we performed the *vsn* in the presence of all

detected proteins. For ratio analysis, normalized abundances of each RP were replicate-matched and divided between different fractions, creating the replicate-specific polysome/total, subpoly/total and sub-poly/poly ratios. Statistical significance of differential protein abundance and ratio values was obtained using a two-sided T-test and Benjamini-Hochberg p-value adjustment. Gene Set Enrichment Analyses and its visualization were performed using the clusterProfiler package [69], for which the genesets were taken from MSigDB v7.0 and gene-ranking metric was selected as log2FC x min(-$\log_{10}$(adj.p-val), 3).

Phosphoproteomics data analysis

For phosphoproteome, data (RAW files) were analyzed by MaxQuant (version 2.0.1.0) [76] using standard settings. MS/MS data were searched using the Swissprot human database (20,395 entries, release 2021_04) complemented with a list of common contaminants and concatenated with the reversed version of all sequences. Trypsin/P was chosen as cleavage specificity allowing two missed cleavages. Carbamidomethylation (C) was set as a fixed modification, while oxidation (M) and phosphorylation(S,T,Y) were used as variable modifications. LFQ intensities were Log_2-transformed in Perseus (version 1.6.15.0) [66], after which the phosphosites were filtered for at least two valid values (out of 3 total) in at least one condition. The values were normalized by subtracting the median per sample. Missing values were replaced by imputation based on a normal distribution using a width of 0.3 and a downshift of 1.8. Differentially regulated phosphosites were determined using a t-test (threshold:–log(p-value) ≥ 1.3 and [x-y] ≥ 1 | [x-y] ≤ -1).

Ribo-seq data analysis

Sequencing data from Ribo-seq experiments was first adapter-trimmed using the cutadapt tool [77], then, after cleaning rRNA & tRNA fragments, remaining reads were mapped to hg38 genome using the STAR aligner [78]. QC plot (RPF length and periodicity) generation and translated ORF predictions were performed with RiboCode [79] using the gencode v34 annotation. Differential analysis of ORF abundances was performed with the DESEQ2 package [68] in the R environment, where ORF-mapping reads were quantified with the Rsubread package [80]. Gene Set Enrichment Analyses were performed with the clusterProfiler [69] package using the log2FC x min(-$\log_{10}$(p-value),5) measure when ranking genes. For the codon level analysis of ribosome occupancy (RO) around transmembrane domain (TMD) ends, TMD coordinates were retrieved from ENSEMBL96 annotation. Focusing only on primary transcripts (based on APPRIS annotation), sample-specific ribosome P-site occupancies (position 12-14 within RPF) were counted at each codon distance from the reference coordinates using a custom python script. For the figure, distance-specific RO

changes were calculated as logFC between two groups, based on group-specific replicate-averaged normalized read count sum across all given reference coordinates, and plotted using a custom R script. Transmembrane domains and signal sequences were identified using the InterPro database (https://www.ebi.ac.uk/interpro/).

TCGA data analysis

Gene expression (HTSeq FPKM) values for all TCGA cohorts were downloaded via UCSC Xena project [35]. For each cohort, sample-specific geneset signature scores were computed as normalized enrichment scores using the ssGSEA method. For each sample, relative RP expression values were obtained with a z-score transformation of raw FPKM values of all ribosomal proteins, excluding the ribosomal protein pseudogenes. All data handling and plotting were performed with a custom R script.

References

1. Hanahan, D. (2022). Hallmarks of Cancer: New Dimensions. Cancer Discov. *12*, 31–46. https://doi.org/10.1158/2159-8290.cd-21-1059.
2. Waldman, A.D., Fritz, J.M., and Lenardo, M.J. (2020). A guide to cancer immunotherapy: from T cell basic science to clinical practice. Nat. Rev. Immunol. *20*, 651–668. https://doi.org/10.1038/s41577-020-0306-5.
3. Zhou, X., Ni, Y., Liang, X., Lin, Y., An, B., He, X., and Zhao, X. (2022). Mechanisms of tumor resistance to immune checkpoint blockade and combination strategies to overcome resistance. Front. Immunol. *13*, 915094. https://doi.org/10.3389/fimmu.2022.915094.
4. Bagaev, A., Kotlov, N., Nomie, K., Svekolkin, V., Gafurov, A., Isaeva, O., Osokin, N., Kozlov, I., Frenkel, F., Gancharova, O., et al. (2021). Conserved pan-cancer microenvironment subtypes predict response to immunotherapy. Cancer Cell *39*, 845-865.e7. https://doi.org/10.1016/j.ccell.2021.04.014.
5. Tray, N., Weber, J.S., and Adams, S. (2018). Predictive Biomarkers for Checkpoint Immunotherapy: Current Status and Challenges for Clinical Application. Cancer Immunol. Res. *6*, 1122–1128. https://doi.org/10.1158/2326-6066.cir-18-0214.
6. Romagnani, S. (2006). Regulation of the T cell response. Clin. Exp. Allergy *36*, 1357–1366. https://doi.org/10.1111/j.1365-2222.2006.02606.x.
7. Kono, H., and Rock, K.L. (2008). How dying cells alert the immune system to danger. Nat. Rev. Immunol. *8*, 279–289. https://doi.org/10.1038/nri2215.
8. Briukhovetska, D., Dörr, J., Endres, S., Libby, P., Dinarello, C.A., and Kobold, S. (2021). Interleukins in cancer: from biology to therapy. Nat. Rev. Cancer *21*, 481–499. https://doi.org/10.1038/s41568-021-00363-z.
9. Nakamura, K., and Smyth, M.J. (2020). Myeloid immunosuppression and immune checkpoints in the tumor microenvironment. Cell. Mol. Immunol. *17*, 1–12. https://doi.org/10.1038/s41423-019-0306-1.
10. Savan, R. (2014). Post-Transcriptional Regulation of Interferons and Their Signaling Pathways. J. Interf. Cytokine Res. *34*, 318–329. https://doi.org/10.1089/jir.2013.0117.
11. Arif, A., Yao, P., Terenzi, F., Jia, J., Ray, P.S., and Fox, P.L. (2018). The GAIT translational control system. Wiley Interdiscip. Rev.: RNA *9*, e1441. https://doi.org/10.1002/wrna.1441.
12. Zhang, Q., and Cao, X. (2019). Epigenetic regulation of the innate immune response to infection. Nat. Rev. Immunol. *19*, 417–432. https://doi.org/10.1038/s41577-019-0151-6.
13. Mauro, V.P., and Edelman, G.M. (2002). The ribosome filter hypothesis. Proc National Acad Sci *99*, 12031–12036. https://doi.org/10.1073/pnas.192442499.
14. Yewdell, J. (2002). To DRiP or not to DRiP: generating peptide ligands for MHC class I molecules from biosynthesized proteins. Mol Immunol *39*, 139–146. https://doi.org/10.1016/s0161-5890(02)00097-4.

15. Genuth, N.R., and Barna, M. (2018). The Discovery of Ribosome Heterogeneity and Its Implications for Gene Regulation and Organismal Life. Mol Cell *71*, 364–374. https://doi.org/10.1016/j.molcel.2018.07.018.
16. Norris, K., Hopes, T., and Aspden, J.L. (2021). Ribosome heterogeneity and specialization in development. Wiley Interdiscip Rev Rna *12*, e1644. https://doi.org/10.1002/wrna.1644.
17. Shi, Z., Fujii, K., Kovary, K.M., Genuth, N.R., Röst, H.L., Teruel, M.N., and Barna, M. (2017). Heterogeneous Ribosomes Preferentially Translate Distinct Subpools of mRNAs Genome-wide. Mol Cell *67*, 71-83.e7. https://doi.org/10.1016/j.molcel.2017.05.021.
18. Parks, M.M., Kurylo, C.M., Dass, R.A., Bojmar, L., Lyden, D., Vincent, C.T., and Blanchard, S.C. (2018). Variant ribosomal RNA alleles are conserved and exhibit tissue-specific expression. Sci Adv *4*, eaao0665. https://doi.org/10.1126/sciadv.aao0665.
19. Jansson, M.D., Häfner, S.J., Altinel, K., Tehler, D., Krogh, N., Jakobsen, E., Andersen, J.V., Andersen, K.L., Schoof, E.M., Ménard, P., et al. (2021). Regulation of translation by site-specific ribosomal RNA methylation. Nat Struct Mol Biol *28*, 889–899. https://doi.org/10.1038/s41594-021-00669-4.
20. Leipold, R.J., and Dhurjati, P. (1993). Specialized Ribosomes in Escherichia coli. Biotechnol Progr *9*, 443–449. https://doi.org/10.1021/bp00023a001.
21. Gebauer, F., and Hentze, M.W. (2004). Molecular mechanisms of translational control. Nat. Rev. Mol. Cell Biol. *5*, 827–835. https://doi.org/10.1038/nrm1488.
22. Genuth, N.R., Shi, Z., Kunimoto, K., Hung, V., Xu, A.F., Kerr, C.H., Tiu, G.C., Oses-Prieto, J.A., Salomon-Shulman, R.E.A., Axelrod, J.D., et al. (2022). A stem cell roadmap of ribosome heterogeneity reveals a function for RPL10A in mesoderm production. Nat Commun *13*, 5491. https://doi.org/10.1038/s41467-022-33263-3.
23. Chen, C., Peng, J., Ma, S., Ding, Y., Huang, T., Zhao, S., Gao, L., Liang, X., Li, C., and Ma, C. (2021). Ribosomal protein S26 serves as a checkpoint of T-cell survival and homeostasis in a p53-dependent manner. Cell. Mol. Immunol. *18*, 1844–1846. https://doi.org/10.1038/s41423-021-00699-4.
24. Stadanlick, J.E., Zhang, Z., Lee, S.-Y., Hemann, M., Biery, M., Carleton, M.O., Zambetti, G.P., Anderson, S.J., Oravecz, T., and Wiest, D.L. (2011). Developmental Arrest of T Cells in Rpl22-Deficient Mice Is Dependent upon Multiple p53 Effectors. J. Immunol. *187*, 664–675. https://doi.org/10.4049/jimmunol.1100029.
25. Zhang, Y., O'Leary, M.N., Peri, S., Wang, M., Zha, J., Melov, S., Kappes, D.J., Feng, Q., Rhodes, J., Amieux, P.S., et al. (2017). Ribosomal Proteins Rpl22 and Rpl22l1 Control Morphogenesis by Regulating Pre-mRNA Splicing. Cell Reports *18*, 545–556. https://doi.org/10.1016/j.celrep.2016.12.034.
26. Ceppi, M., Clavarino, G., Gatti, E., Schmidt, E.K., Gassart, A. de, Blankenship, D., Ogola, G., Banchereau, J., Chaussabel, D., and Pierre, P. (2009). Ribosomal protein mRNAs are translationally-regulated during human dendritic cells activation by LPS. Immunome Res *5*, 5. https://doi.org/10.1186/1745-7580-5-5.

27. Fahl, S.P., Harris, B., Coffey, F., and Wiest, D.L. (2015). Rpl22 Loss Impairs the Development of B Lymphocytes by Activating a p53-Dependent Checkpoint. J. Immunol. *194*, 200–209. https://doi.org/10.4049/jimmunol.1402242.

28. Yewdell, J.W., and Nicchitta, C.V. (2006). The DRiP hypothesis decennial: support, controversy, refinement and extension. Trends Immunol *27*, 368–373. https://doi.org/10.1016/j.it.2006.06.008.

29. Wei, J., Kishton, R.J., Angel, M., Conn, C.S., Dalla-Venezia, N., Marcel, V., Vincent, A., Catez, F., Ferré, S., Ayadi, L., et al. (2019). Ribosomal Proteins Regulate MHC Class I Peptide Generation for Immunosurveillance. Mol Cell *73*, 1162-1173.e5. https://doi.org/10.1016/j.molcel.2018.12.020.

30. Grela, P., Krokowski, D., Gordiyenko, Y., Krowarsch, D., Robinson, C.V., Otlewski, J., Grankowski, N., and Tchórzewski, M. (2010). Biophysical Properties of the Eukaryotic Ribosomal Stalk. Biochemistry-us *49*, 924–933. https://doi.org/10.1021/bi901811s.

31. Remacha, M., Santos, C., Bermejo, B., Naranda, T., and Ballesta, J.P. (1992). Stable binding of the eukaryotic acidic phosphoproteins to the ribosome is not an absolute requirement for in vivo protein synthesis. J Biological Chem *267*, 12061–12067.

32. Bautista-Santos, A., and Zinker, S. (2014). The P1/P2 Protein Heterodimers Assemble to the Ribosomal Stalk at the Moment When the Ribosome Is Committed to Translation but Not to the Native 60S Ribosomal Subunit in Saccharomyces cerevisiae. Biochemistry-us *53*, 4105–4112. https://doi.org/10.1021/bi500341w.

33. Patel, S.J., Sanjana, N.E., Kishton, R.J., Eidizadeh, A., Vodnala, S.K., Cam, M., Gartner, J.J., Jia, L., Steinberg, S.M., Yamamoto, T.N., et al. (2017). Identification of essential genes for cancer immunotherapy. Nature *548*, 537–542. https://doi.org/10.1038/nature23477.

34. Harding, H.P., Ordonez, A., Allen, F., Parts, L., Inglis, A.J., Williams, R.L., and Ron, D. (2019). The ribosomal P-stalk couples amino acid starvation to GCN2 activation in mammalian cells. Elife *8*, e50149. https://doi.org/10.7554/elife.50149.

35. Goldman, M.J., Craft, B., Hastie, M., Repečka, K., McDade, F., Kamath, A., Banerjee, A., Luo, Y., Rogers, D., Brooks, A.N., et al. (2020). Visualizing and interpreting cancer genomics data via the Xena platform. Nat Biotechnol *38*, 675–678. https://doi.org/10.1038/s41587-020-0546-8.

36. Ayers, M., Lunceford, J., Nebozhyn, M., Murphy, E., Loboda, A., Kaufman, D.R., Albright, A., Cheng, J.D., Kang, S.P., Shankaran, V., et al. (2017). IFN-γ–related mRNA profile predicts clinical response to PD-1 blockade. J Clin Invest *127*, 2930–2940. https://doi.org/10.1172/jci91190.

37. Bui, T.M., Wiesolek, H.L., and Sumagin, R. (2020). ICAM-1: A master regulator of cellular responses in inflammation, injury resolution, and tumorigenesis. J. Leukoc. Biol. *108*, 787–799. https://doi.org/10.1002/jlb.2mr0220-549r.

38. Vereecke, L., Beyaert, R., and Loo, G. van (2009). The ubiquitin-editing enzyme A20 (TNFAIP3) is a central regulator of immunopathology. Trends Immunol. *30*, 383–391. https://doi.org/10.1016/j.it.2009.05.007.

39. Helgstrand, M., Mandava, C.S., Mulder, F.A.A., Liljas, A., Sanyal, S., and Akke, M. (2007). The Ribosomal Stalk Binds to Translation Factors IF2, EF-Tu, EF-G and RF3 via a Conserved Region of the L12 C-terminal Domain. J. Mol. Biol. *365*, 468–479. https://doi.org/10.1016/j.jmb.2006.10.025.

40. Nomura, N., Honda, T., Baba, K., Naganuma, T., Tanzawa, T., Arisaka, F., Noda, M., Uchiyama, S., Tanaka, I., Yao, M., et al. (2012). Archaeal ribosomal stalk protein interacts with translation factors in a nucleotide-independent manner via its conserved C terminus. Proc. Natl. Acad. Sci. *109*, 3748–3753. https://doi.org/10.1073/pnas.1112934109.

41. Campos, R.K., Wong, B., Xie, X., Lu, Y.-F., Shi, P.-Y., Pompon, J., Garcia-Blanco, M.A., and Bradrick, S.S. (2017). RPLP1 and RPLP2 Are Essential Flavivirus Host Factors That Promote Early Viral Protein Accumulation. J Virol *91*. https://doi.org/10.1128/jvi.01706-16.

42. Campos, R.K., Wijeratne, H.R.S., Shah, P., Garcia-Blanco, M.A., and Bradrick, S.S. (2020). Ribosomal stalk proteins RPLP1 and RPLP2 promote biogenesis of flaviviral and cellular multi-pass transmembrane proteins. Nucleic Acids Res *48*, 9872–9885. https://doi.org/10.1093/nar/gkaa717.

43. Hasler, P., Brot, N., Weissbach, H., Parnassa, A.P., and Elkon, K.B. (1991). Ribosomal proteins P0, P1, and P2 are phosphorylated by casein kinase II at their conserved carboxyl termini. J. Biol. Chem. *266*, 13815–13820. https://doi.org/10.1016/s0021-9258(18)92774-2.

44. Filipek, K., Michalec-Wawiórka, B., Boguszewska, A., Kmiecik, S., and Tchórzewski, M. (2020). Phosphorylation of the N-terminal domain of ribosomal P-stalk protein uL10 governs its association with the ribosome. Febs Lett *594*, 3002–3019. https://doi.org/10.1002/1873-3468.13885.

45. Romero, J.M., Titmuss, E., Wang, Y., Vafiadis, J., Pacis, A., Jang, G.H., Zhang, A., Golesworthy, B., Lenko, T., Williamson, L.M., et al. (2023). Chemokine expression predicts T cell-inflammation and improved survival with checkpoint inhibition across solid cancers. npj Precis. Oncol. *7*, 73. https://doi.org/10.1038/s41698-023-00428-2.

46. Gu, S.S., Zhang, W., Wang, X., Jiang, P., Traugh, N., Li, Z., Meyer, C., Stewig, B., Xie, Y., Bu, X., et al. (2021). Therapeutically Increasing MHC-I Expression Potentiates Immune Checkpoint Blockade. Cancer Discov. *11*, 1524–1541. https://doi.org/10.1158/2159-8290.cd-20-0812.

47. Kawase, K., Kawashima, S., Nagasaki, J., Inozume, T., Tanji, E., Kawazu, M., Hanazawa, T., and Togashi, Y. (2023). High Expression of MHC Class I Overcomes Cancer Immunotherapy Resistance Due to IFNγ Signaling Pathway Defects. Cancer Immunol. Res. *11*, OF1–OF14. https://doi.org/10.1158/2326-6066.cir-22-0815.

48. Blank, C.U., Haanen, J.B., Ribas, A., and Schumacher, T.N. (2016). The “cancer immunogram.” Science *352*, 658–660. https://doi.org/10.1126/science.aaf2834.

49. Peng, D., Kryczek, I., Nagarsheth, N., Zhao, L., Wei, S., Wang, W., Sun, Y., Zhao, E., Vatan, L., Szeliga, W., et al. (2015). Epigenetic silencing of TH1-type chemokines shapes tumour immunity and immunotherapy. Nature *527*, 249–253. https://doi.org/10.1038/nature15520.

50. Silva, R.B. da, Laird, M.E., Yatim, N., Fiette, L., Ingersoll, M.A., and Albert, M.L. (2015). Dipeptidylpeptidase 4 inhibition enhances lymphocyte trafficking, improving both naturally

occurring tumor immunity and immunotherapy. Nat. Immunol. *16*, 850–858. https://doi.org/10.1038/ni.3201.

51. Shiraishi, C., Matsumoto, A., Ichihara, K., Yamamoto, T., Yokoyama, T., Mizoo, T., Hatano, A., Matsumoto, M., Tanaka, Y., Matsuura-Suzuki, E., et al. (2023). RPL3L-containing ribosomes determine translation elongation dynamics required for cardiac function. Nat Commun *14*, 2131. https://doi.org/10.1038/s41467-023-37838-6.
52. Fusco, C.M., Desch, K., Dörrbaum, A.R., Wang, M., Staab, A., Chan, I.C.W., Vail, E., Villeri, V., Langer, J.D., and Schuman, E.M. (2021). Neuronal ribosomes exhibit dynamic and context-dependent exchange of ribosomal proteins. Nat Commun *12*, 6127. https://doi.org/10.1038/s41467-021-26365-x.
53. Hopes, T., Norris, K., Agapiou, M., McCarthy, C.G.P., Lewis, P.A., O'Connell, M.J., Fontana, J., and Aspden, J.L. (2022). Ribosome heterogeneity in Drosophila melanogaster gonads through paralog-switching. Nucleic Acids Res *50*, 2240–2257. https://doi.org/10.1093/nar/gkab606.
54. Milenkovic, I., Santos Vieira, H.G., Lucas, M.C., Ruiz-Orera, J., Patone, G., Kesteven, S., Wu, J., Feneley, M., Espadas, G., Sabidó, E., et al. (2023). Dynamic interplay between RPL3- and RPL3L-containing ribosomes modulates mitochondrial activity in the mammalian heart. Nucleic Acids Res. https://doi.org/10.1093/nar/gkad121.
55. Remacha, M., Jimenez-Diaz, A., Santos, C., Briones, E., Zambrano, R., Gabriel, M.A.R., Guarinos, E., and Ballesta, J.P.G. (1995). Proteins P1, P2, and P0, components of the eukaryotic ribosome stalk. New structural and functional aspects. Biochem. Cell Biol. *73*, 959–968. https://doi.org/10.1139/o95-103.
56. Mayr, C. (2019). What Are 3′ UTRs Doing? Csh Perspect Biol *11*, a034728. https://doi.org/10.1101/cshperspect.a034728.
57. Yewdell, J.W., Dersh, D., and Fåhraeus, R. (2019). Peptide Channeling: The Key to MHC Class I Immunosurveillance? Trends Cell Biol *29*, 929–939. https://doi.org/10.1016/j.tcb.2019.09.004.
58. Shimizu, T., Nakagaki, M., Nishi, Y., Kobayashi, Y., Hachimori, A., and Uchiumi, T. (2002). Interaction among silkworm ribosomal proteins P1, P2 and P0 required for functional protein binding to the GTPase-associated domain of 28S rRNA. Nucleic Acids Res. *30*, 2620–2627. https://doi.org/10.1093/nar/gkf379.
59. Uchiumi, T., Honma, S., Nomura, T., Dabbs, E.R., and Hachimori, A. (2002). Translation Elongation by a Hybrid Ribosome in Which Proteins at the GTPase Center of the Escherichia coli Ribosome Are Replaced with Rat Counterparts*. J. Biol. Chem. *277*, 3857–3862. https://doi.org/10.1074/jbc.m107730200.
60. Ishimura, R., Nagy, G., Dotu, I., Chuang, J.H., and Ackerman, S.L. (2016). Activation of GCN2 kinase by ribosome stalling links translation elongation with translation initiation. Elife *5*, e14295. https://doi.org/10.7554/elife.14295.
61. Wolin, S.L., and Walter, P. (1988). Ribosome pausing and stacking during translation of a eukaryotic mRNA. EMBO J. *7*, 3559–3569. https://doi.org/10.1002/j.1460-2075.1988.tb03233.x.

62. Phillips, B.P., and Miller, E.A. (2020). Ribosome-associated quality control of membrane proteins at the endoplasmic reticulum. J. Cell Sci. *133*, jcs251983. https://doi.org/10.1242/jcs.251983.

63. Gawroński, P., Jensen, P.E., Karpiński, S., Leister, D., and Scharff, L.B. (2018). Pausing of Chloroplast Ribosomes Is Induced by Multiple Features and Is Linked to the Assembly of Photosynthetic Complexes . Plant Physiol. *176*, 2557–2569. https://doi.org/10.1104/pp.17.01564.

64. Gomez-Eerland, R., Nuijen, B., Heemskerk, B., Rooij, N. van, Berg, J.H. van den, Beijnen, J.H., Uckert, W., Kvistborg, P., Schumacher, T.N., Haanen, J.B.A.G., et al. (2014). Manufacture of Gene-Modified Human T-Cells with a Memory Stem/Central Memory Phenotype. Hum Gene Ther Method *25*, 277–287. https://doi.org/10.1089/hgtb.2014.004.

65. Silva, J., Alkan, F., Ramalho, S., Snieckute, G., Prekovic, S., Garcia, A.K., Hernández-Pérez, S., Kammen, R. van der, Barnum, D., Hoekman, L., et al. (2022). Ribosome impairment regulates intestinal stem cell identity via ZAKα activation. Nat Commun *13*, 4492. https://doi.org/10.1038/s41467-022-32220-4.

66. Link, A.J., and LaBaer, J. (2011). Trichloroacetic Acid (TCA) Precipitation of Proteins. Cold Spring Harb Protoc *2011*, pdb.prot5651. https://doi.org/10.1101/pdb.prot5651.

67. Jersie-Christensen, R.R., Sultan, A., and Olsen, J.V. (2015). Phospho-Proteomics, Methods and Protocols. Methods Mol. Biol. *1355*, 251–260. https://doi.org/10.1007/978-1-4939-3049-4_17.

68. Demichev, V., Messner, C.B., Vernardis, S.I., Lilley, K.S., and Ralser, M. (2020). DIA-NN: neural networks and interference correction enable deep proteome coverage in high throughput. Nat Methods *17*, 41–44. https://doi.org/10.1038/s41592-019-0638-x.

69. Tyanova, S., Temu, T., Sinitcyn, P., Carlson, A., Hein, M.Y., Geiger, T., Mann, M., and Cox, J. (2016). The Perseus computational platform for comprehensive analysis of (prote)omics data. Nat Methods *13*, 731–740. https://doi.org/10.1038/nmeth.3901.

70. Huber, W., Heydebreck, A. von, Sültmann, H., Poustka, A., and Vingron, M. (2002). Variance stabilization applied to microarray data calibration and to the quantification of differential expression. Bioinformatics *18*, S96–S104. https://doi.org/10.1093/bioinformatics/18.suppl_1.s96.

71. Yu, G., Wang, L.-G., Han, Y., and He, Q.-Y. (2012). clusterProfiler: an R Package for Comparing Biological Themes Among Gene Clusters. Omics J Integr Biology *16*, 284–287. https://doi.org/10.1089/omi.2011.0118.

72. Cox, J., Hein, M.Y., Luber, C.A., Paron, I., Nagaraj, N., and Mann, M. (2014). Accurate Proteome-wide Label-free Quantification by Delayed Normalization and Maximal Peptide Ratio Extraction, Termed MaxLFQ. Mol Cell Proteomics *13*, 2513–2526. https://doi.org/10.1074/mcp.m113.031591.

73. Ingolia, N.T., Brar, G.A., Rouskin, S., McGeachy, A.M., and Weissman, J.S. (2012). The ribosome profiling strategy for monitoring translation in vivo by deep sequencing of ribosome-protected mRNA fragments. Nat Protoc *7*, 1534–1550. https://doi.org/10.1038/nprot.2012.086.

74. Martin, M. (2011). Cutadapt removes adapter sequences from high-throughput sequencing reads. Embnet J *17*, 10–12. https://doi.org/10.14806/ej.17.1.200.

75. Dobin, A., Davis, C.A., Schlesinger, F., Drenkow, J., Zaleski, C., Jha, S., Batut, P., Chaisson, M., and Gingeras, T.R. (2013). STAR: ultrafast universal RNA-seq aligner. Bioinformatics *29*, 15–21. https://doi.org/10.1093/bioinformatics/bts635.

76. Xiao, Z., Huang, R., Xing, X., Chen, Y., Deng, H., and Yang, X. (2018). De novo annotation and characterization of the translatome with ribosome profiling data. Nucleic Acids Res *46*, gky179-. https://doi.org/10.1093/nar/gky179.

77. Love, M.I., Huber, W., and Anders, S. (2014). Moderated estimation of fold change and dispersion for RNA-seq data with DESeq2. Genome Biol *15*, 550. https://doi.org/10.1186/s13059-014-0550-8.

78. Liao, Y., Smyth, G.K., and Shi, W. (2019). The R package Rsubread is easier, faster, cheaper and better for alignment and quantification of RNA sequencing reads. Nucleic Acids Res *47*, gkz114-. https://doi.org/10.1093/nar/gkz114.

79. Taranto, D., et al., Multiparametric Analyses of Hepatocellular Carcinoma Somatic Mouse Models and Their Associated Tumor Microenvironment. Curr Protoc, 2021. **1**(6): p. e147.

Extended data

Data S1: Quality control experiments for P1 knockdown, flow cytometry and ribosome profiling

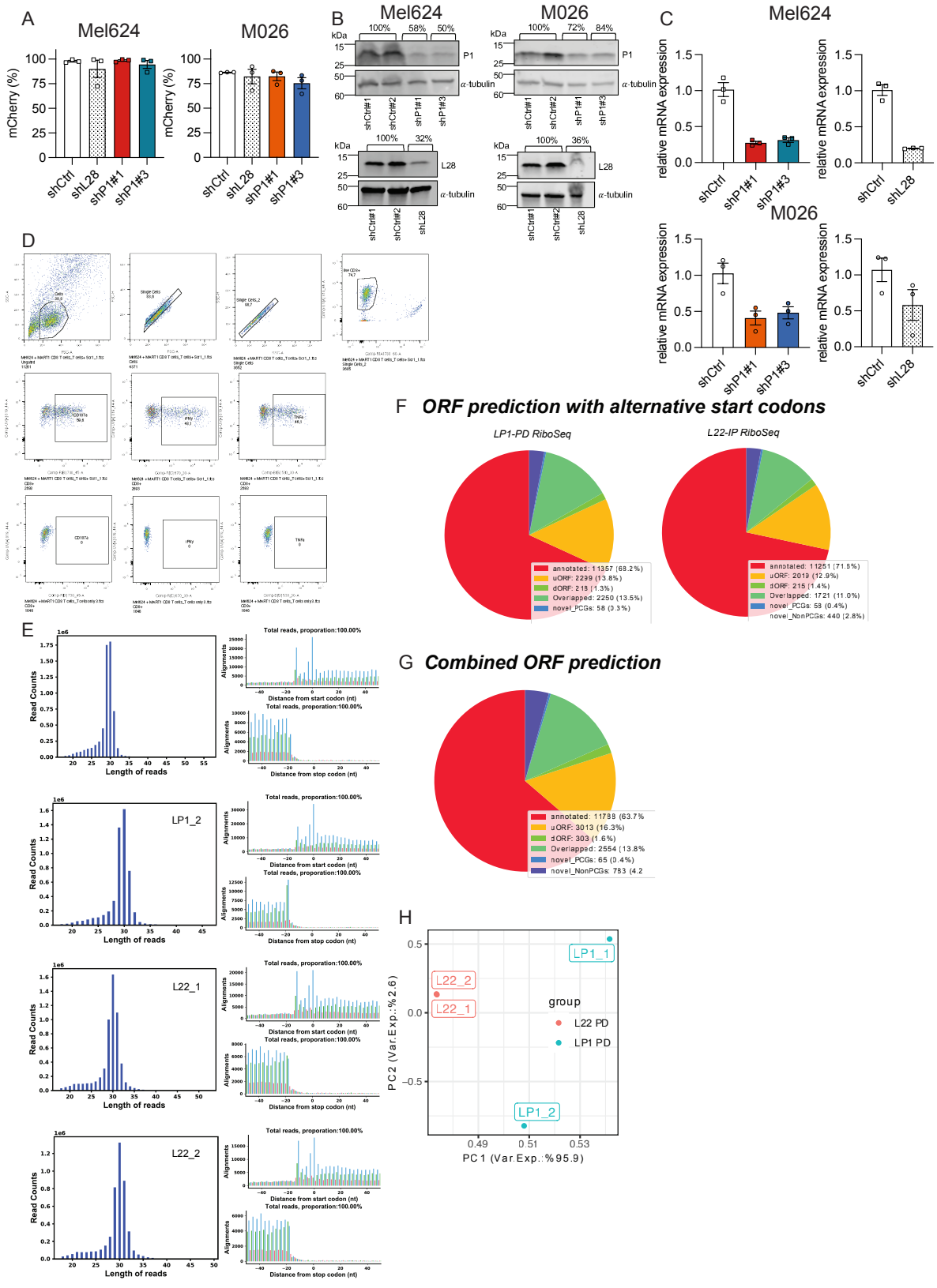

Data S1. [legend on the next page]

Data S1 [previous page]. Quality control experiments for P1 knockdown, flow cytometry, and ribosome profiling, related to Figures 2 and 3

(**A**) Transduction efficiency was measured by flow cytometry using mCherry (%) expression gated on live tumor cells. *n* = 3 independent experiments per cell line, each assessed in triplicates, represented as mean ± SEM.

(**B**) Western blot analysis confirming efficient RP KD in Mel624 and M026 tumor cells. α-tubulin was used as loading control. *n* = 1 experiment per cell line.

(**C**) RT-qPCR analysis confirming efficient RP KD using *ACTB* as a reference. *n* = 3 technical replicates, represented as mean ± SD.

(**D**). Representation of co-culture gating strategy.

(**E**) Ribo-seq quality control plots showing the length distribution and periodicity of sequenced ribosome protected fragments in our Ribo-seq experiments.

(**F**) Pie chart showing the distribution of predicted ORF classes performed by RiboCode separately on P1-PD and L22-PD Ribo-seq data, allowing alternative start codons.

(**G**) Predicted ORF class distribution performed by RiboCode jointly on all Ribo-seq samples, allowing only ATG start codon.

(**H**) PCA with ORF-mapping read quantifications for which Ribo-seq reads were quantified by the subread package on ORFs.

Supplementary figures

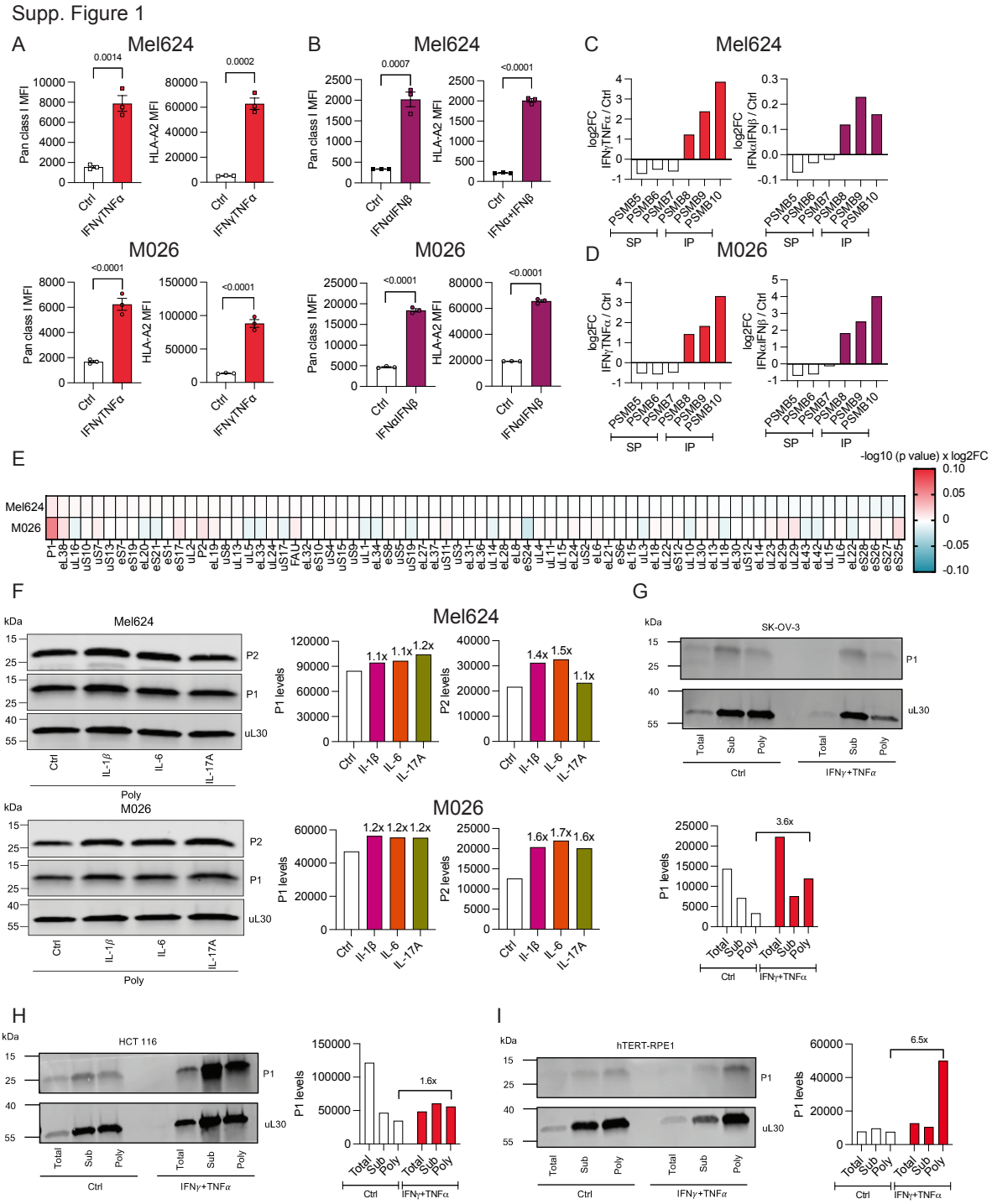

Figure S1. [legend on the next page]

Figure S1 [previous page]. Cytokine exposure induces an alert state in tumor cells and increases P-stalk incorporation, related to Figure 1

(**A**) IFNγ/TNF-α treatment upregulates HLA I surface levels in Mel624 and M026 tumor cells. HLA levels were measured by flow cytometry using MFI. *n* = 3 independent experiments per cell line, each assessed in triplicates represented as mean ± SEM. *p* values were calculated using a two-tailed t test.

(**B**) IFNα/IFNβ treatment upregulates HLA I surface levels in tumor cells. HLA levels were measured by flow cytometry using MFI. *n* = 3 independent experiments per cell line, each assessed in triplicates represented as mean ± SEM. *p* values were calculated using a two-tailed t test.

(**C**) IFNγ/TNF-α and IFNα/IFNβ treatment increases immunoproteasome subunits (IP; PSMB8, PSMB9, and PSMB10) compared with standard proteasome subunits (SP; PSMB5, PSMB6, and PSMB7) in Mel624 tumor cells. *n* = 3 independent experiments represented as mean.

(**D**) IFNγ/TNF-α and IFNα/IFNβ treatment increases immunoproteasome subunits (IP; PSMB8, PSMB9, and PSMB10) compared with standard proteasome subunits (SP; PSMB5, PSMB6, and PSMB7) in M026 tumor cells. *n* = 3 independent experiments represented as mean.

(**E**) P1 association with the translating ribosome (poly) is increased upon IFNα/IFNβ exposure in Mel624 and M026 tumor cells. Heatmap shows polysome to total ratio in cytokine-treated vs. untreated cells. *n* = 3 independent experiments.

(**F**) Western blot analysis confirming increased polysomal association of P1 and P2 upon exposure to IL-1β, IL-6, and IL-17A in Mel624 and M026 tumor cells. uL30 was used as control RP for data normalization. *n* = 1 experiment per cell line.

(**G–I**) Western blot analysis confirms increased polysomal association of P1 upon IFNγ/TNF-α stimulation in SK-OV-3 (G), HCT 116 (H), and hTERT-RPE1 (I) cells. uL30 was used as control RP for data normalization. *n* = 1 experiment per cell line.

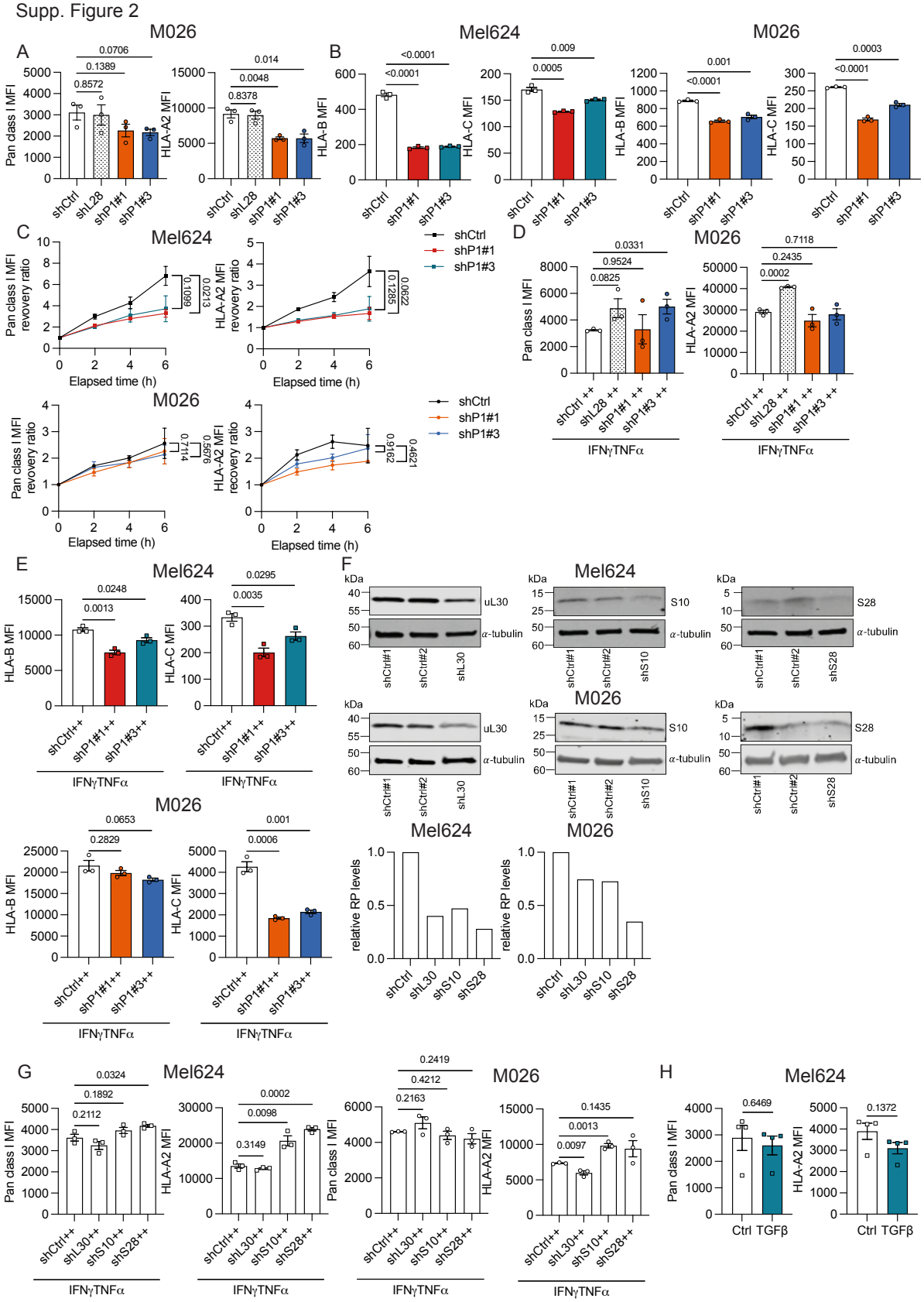

Figure S2. [legend on the next page]

Figure S2 [previous page]. The PSR regulates HLA I levels and cytokine-mediated processes, related to Figure 2

(**A**) P1 KD decreases HLA I surface levels in M026 cells. *n* = 3 independent experiments, each assessed in triplicates. Data are represented as mean ± SEM, and *p* values were determined using a two-tailed t test.

(**B**) P1 KD decreases HLA-B and HLA-C surface levels in Mel624 and M026 cells. *n* = 3 independent experiments per cell line. Data are represented as mean ± SEM, and *p* values were determined using a two-tailed t test.

(**C**) shP1 Mel624 and M026 tumor cells show slower recovery kinetics of HLA I after acid wash compared with the control. *n* = 3 independent experiments. Data are represented as mean ± SEM.

(**D**) Exposure to IFNγ/TNF-α results in attenuated HLA I surface levels in shP1 M026 tumor cells. *n* = 3 biological replicates represented as mean ± SEM. *p* values were calculated using a two-tailed t test.

(**E**) Exposure to IFNγ/TNF-α results in attenuated HLA-B and HLA-C surface levels in shP1 Mel624 and M026 tumor cells. *n* = 3 biological replicates represented as mean ± SEM. *p* values were calculated using a two-tailed t test.

(**F**) Western blot analysis confirming efficient KD of uL30, eS10, and eS28 in M026 and Mel624 tumor cells. α-tubulin was used as loading control. *n* = 1 experiment per cell line.

(**G**) KD of uL30, eS10, and eS28 exposed to IFNγ/TNF-α does not affect HLA I surface levels in Mel624 and M026 tumor cells. *n* = 3 biological replicates represented as mean ± SEM. *p* values were calculated using a two-tailed t test.

(**H**) TGF-β decreases HLA I surface levels in tumor cells. *n* = 4 biological replicates. Data are represented as mean ± SEM, and *p* values were determined using a two-tailed t test.

Supp. Figure 3

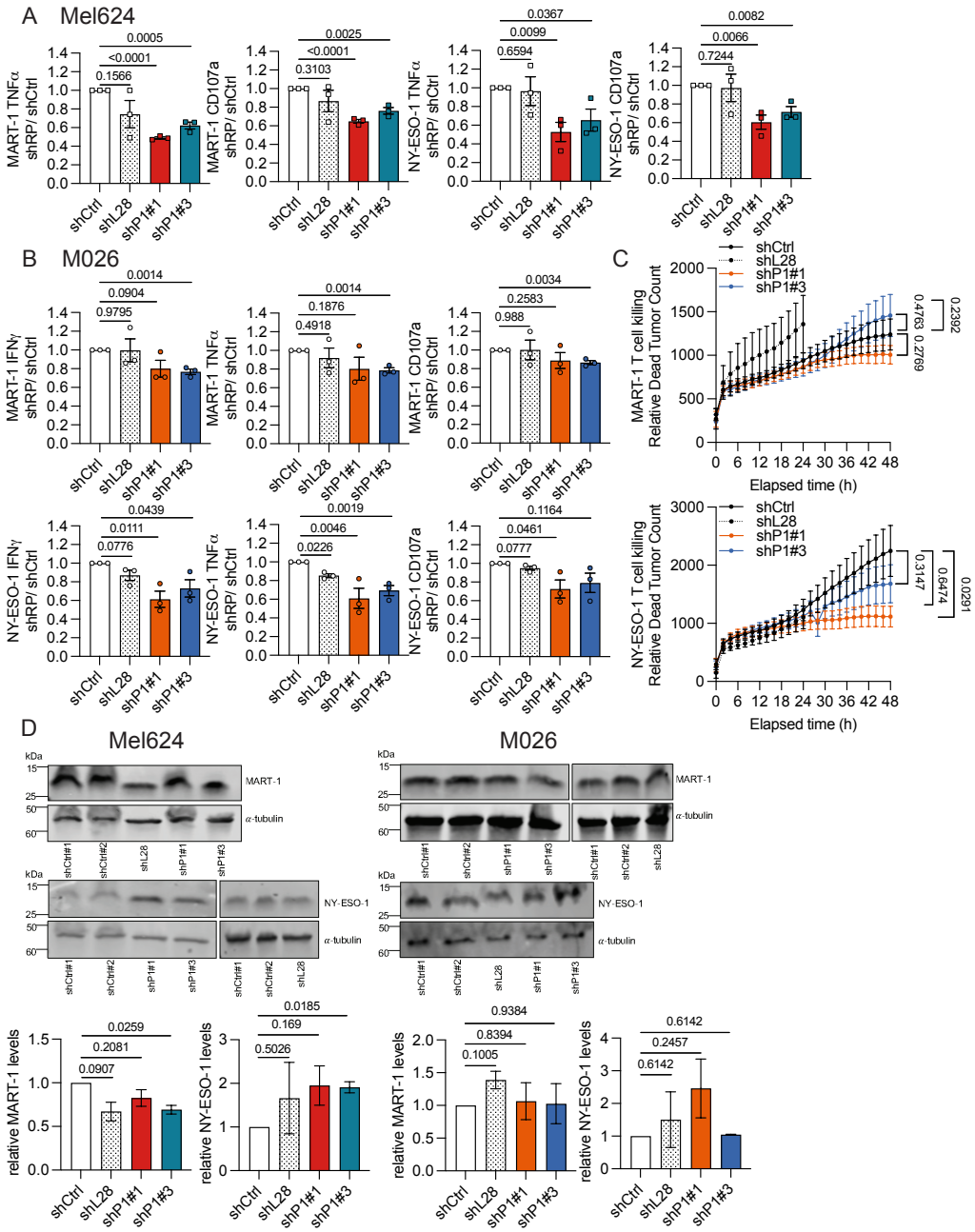

Figure S3. The PSR is important for T cell recognition and killing, related to Figure 2

(**A**) MART-1 and NY-ESO-1-specific CD8$^+$ T cell recognition is decreased in shP1 compared with control Mel624 tumor cells. *n* = 3 independent experiments, each assessed in triplicates. Data are represented as mean ± SEM, and *p* values relative to shCtrl were determined using a two-tailed t test.

(**B**) MART-1 and NY-ESO-1-specific CD8$^+$ T cell recognition is decreased in shP1 compared with control M026 tumor cells. *n* = 3 independent experiments, each assessed in triplicates. Data are represented as mean ± SEM, and *p* values relative to shCtrl were determined using a two-tailed t test.

(**C**) MART-1 and NY-ESO-1-specific $CD8^+$ T cell killing is attenuated in shP1 M026 tumor cells. *n* = 3 independent experiments per cell line, each assessed in triplicates. Data represent mean and error ± SEM, and *p* values were calculated with a two-tailed t test.

(**D**) Western blot showing unaltered MART-1 and NY-ESO-1 source protein levels upon P1 KD in Mel624 and M026 cells. α-tubulin was used as loading control. *n* = 2 independent experiments represented as mean ± SEM, and *p* values were calculated with a two-tailed t test.

Supp. Figure 4

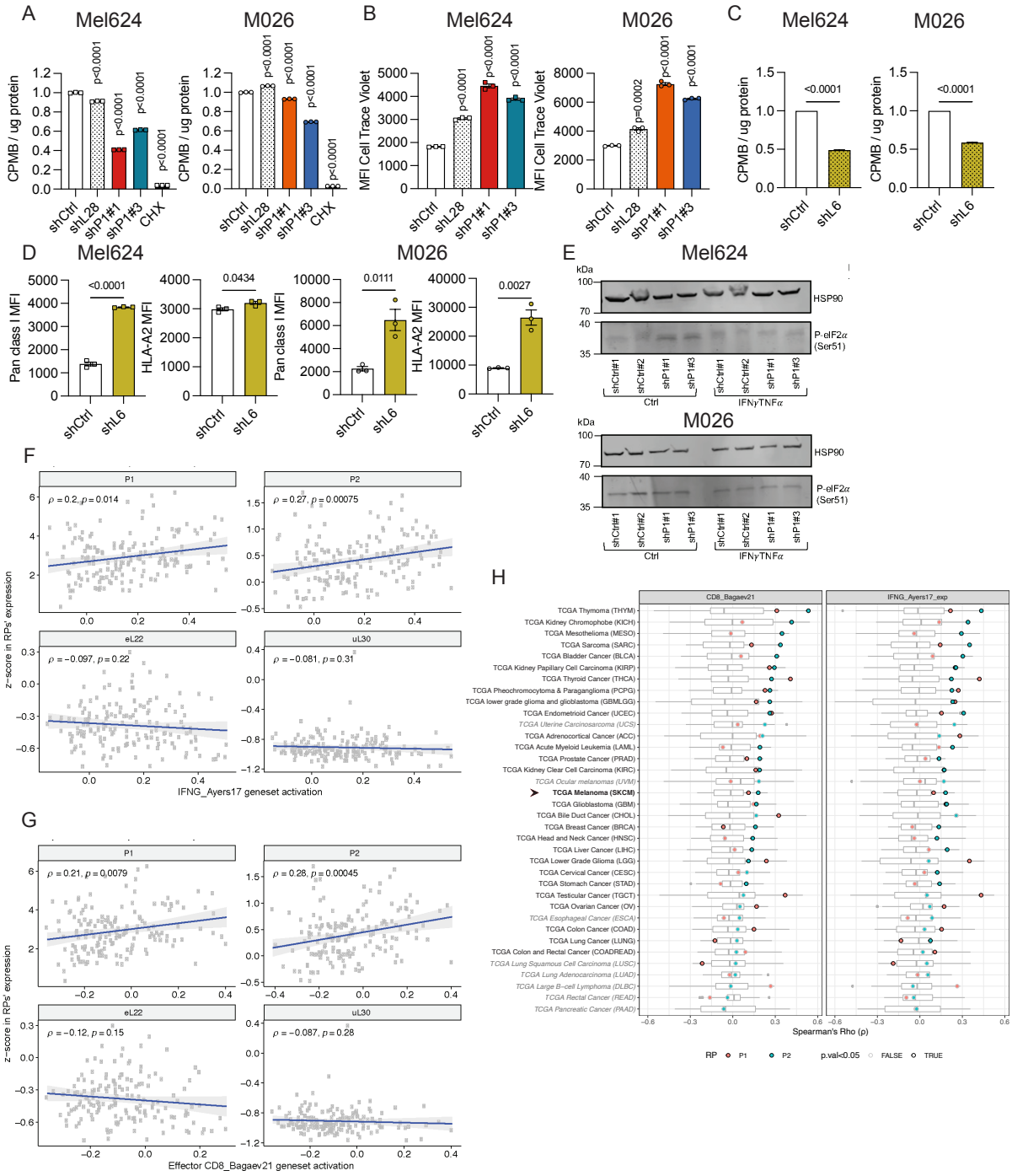

Figure S4. [legend on the next page]

Figure S4 [previous page]. P-stalk does not regulate APP through a general inhibition of translation, and P-stalk levels correlate with T cell response across diverse tissues, related to Figure 3

(**A**) ^{35}S-methionine incorporation assay showing decreased protein synthesis upon P1 KD in Mel624 and M026 cells. Cycloheximide (CHX) was used as a control to inhibit protein synthesis. *n* = 3 technical replicates represented as mean ± SD. *p* values were calculated using a two-tailed t test.

(**B**) CellTrace violet cell proliferation assay showing decreased cell proliferation upon P1 KD in M026 and Mel624 cells. Proliferation was assessed by flow cytometry using the MFI. *n* = 3 biological replicates represented as mean ± SEM. *p* values were calculated using a two-tailed t test.

(**C**) ^{35}S-methionine incorporation assay showing inhibited protein synthesis in Mel624 and M026 cells following eL6 KD, similar to P1 KD. *n* = 3 technical replicates represented as mean ± SD. *p* values were determined using a two-tailed t test.

(**D**) Translation inhibition caused by KD of eL6 shows minor effects on HLA I surface levels in Mel624 and M026 tumor cells. *n* = 3 biological replicates represented as mean ± SEM. *p* values were calculated using a two-tailed t test.

(**E**) Western blot analysis showing no increase of eIF2α phosphorylation following P1 KD, with or without IFNγ/TNF-α. HSP90 was used as loading control. *n* = 1 experiment per cell line.

(**F**) TCGA-SKCM melanoma cohort gene expression analysis reveals a significant correlation between P1 and P2 but not eL22 or uL30 relative expression levels and IFNγ response signature. *p* values were calculated using Spearman's rank correlation. *n* = 474.

(**G**) TCGA-SKCM melanoma cohort gene expression analysis reveals a significant correlation between P1 and P2 but not eL22 or uL30 relative expression levels (Z score of FPKM values within all RPs) and effector CD8 T cell infiltration. *p* values were calculated using Spearman's rank correlation. *n* = 474.

(**H**) Correlation analyses of TGCA cohorts (*n* = 36) and all RPs (*n* = 90) reveal a significant correlation between relative P-stalk expression (Z score) and IFNγ response signature and effector CD8 T cell infiltration in diverse tissues. Box plots represent the distribution of RP-specific correlation coefficients (Spearman's rho). Significant correlations ($p < 0.05$) are circled in black.

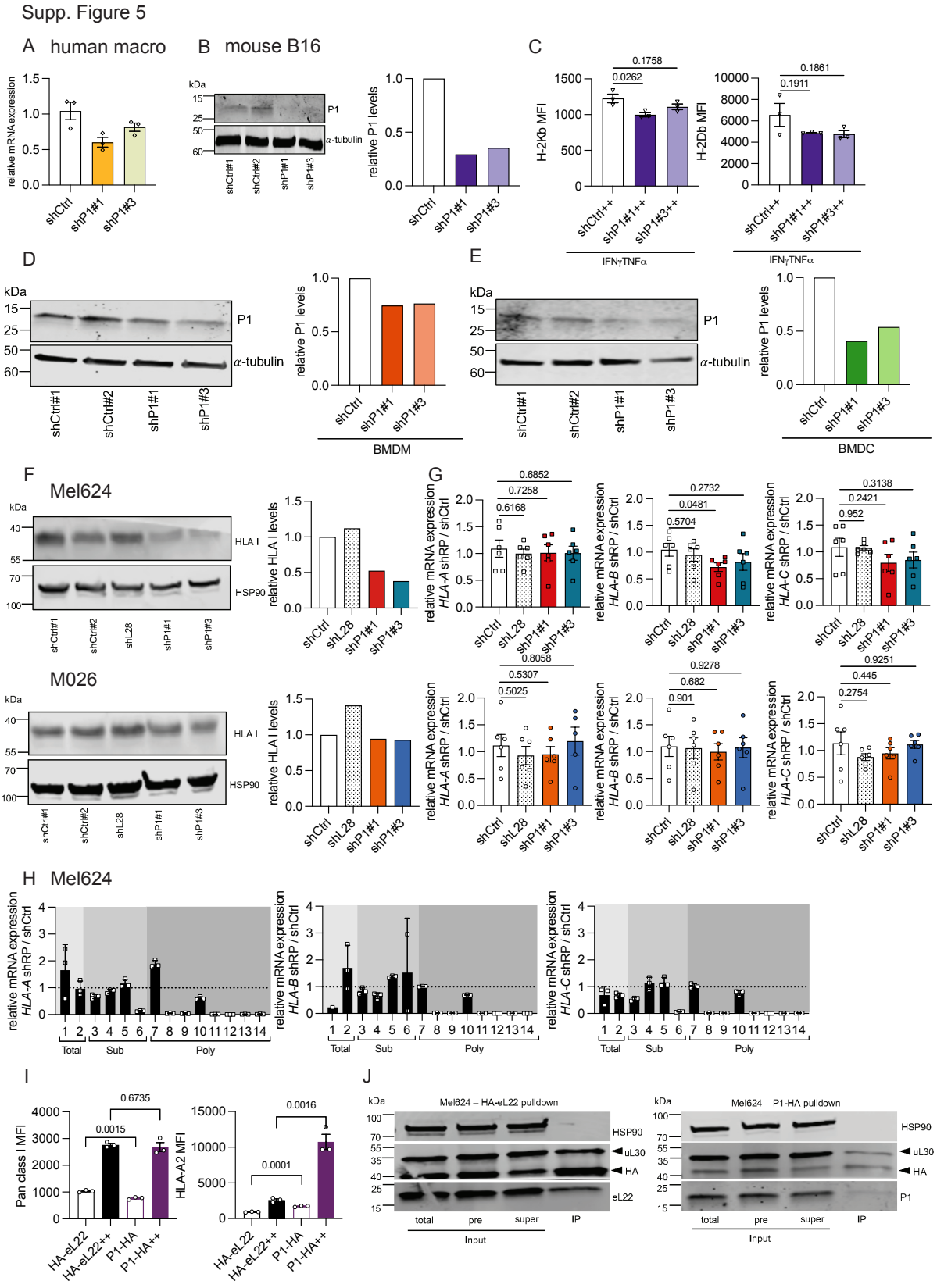

Figure S5. [legend on the next page]

Figure S5 [previous page]. The PSR translates mRNAs important for immunosurveillance, related to Figure 3

(**A**) RT-qPCR analysis confirming efficient P1 KD in human PBMC-derived macrophages, using *ACTB* as a reference. *n* = 3 technical replicates represented as mean ± SD.

(**B**) Western blot analysis confirming efficient P1 KD in mouse B16 melanoma cells. α-tubulin was used as loading control. *n* = 1 experiment.

(**C**) Exposure to IFNγ/TNF-α results in attenuated H-2Kb and H-2Db surface levels in shP1 mouse B16 melanoma cells compared with the control. *n* = 3 biological replicates represented as mean ± SEM. *p* values were calculated using a two-tailed t test.

(**D**) Western blot analysis confirming efficient P1 KD in mouse BMDMs. α-tubulin was used as loading control. *n* = 1 experiment.

(**E**) Western blot analysis confirming efficient P1 KD in mouse BMDCs. α-tubulin was used as loading control. *n* = 1 experiment.

(**F**) Western blot demonstrating a decrease in HLA I protein levels in shP1 compared with control Mel624 and M026 tumor cells. HSP90 was used as loading control. *n* = 1 experiment per cell line.

(**G**) RT-qPCR showing no change in HLA mRNA levels (*HLA-A*, *HLA-B*, and *HLA-C*) following P1 KD in Mel624 and M026 tumor cells, using *ACTB* as a reference. *n* = 6 technical replicates. Data are represented as mean ± SEM, and *p* values were determined using a two-tailed t test.

(**H**) RT-qPCR of isolated fraction 1–14 showing decreased polysomal association of HLA mRNA in shP1 cells, using *ACTB* as a reference. *n* = 3 technical replicates represented as mean ± SD.

(**I**) PSR overexpression increases HLA I surface levels in untreated (P1-HA, HA-eL22) and IFNγ/TNF-α treated (P1-HA++, HA-eL22++) tumor cells. HLA levels were assessed by flow cytometry using the MFI. *n* = 3 independent experiments. Data are represented as mean ± SEM, and *p* values were determined using a two-tailed t test.

(**J**) Western blot confirming the expression of tagged HA-eL22 and P1-HA (input: total, pre-clearance [pre], supernatant [super]) and isolation of eL22- and P1-containing ribosomes (immunoprecipitation [IP]) in Mel624 tumor cells. CoIP of uL30 was used as a control for pull-down of intact ribosomes, and HSP90 was used as loading control. *n* = 1 replicate per condition.

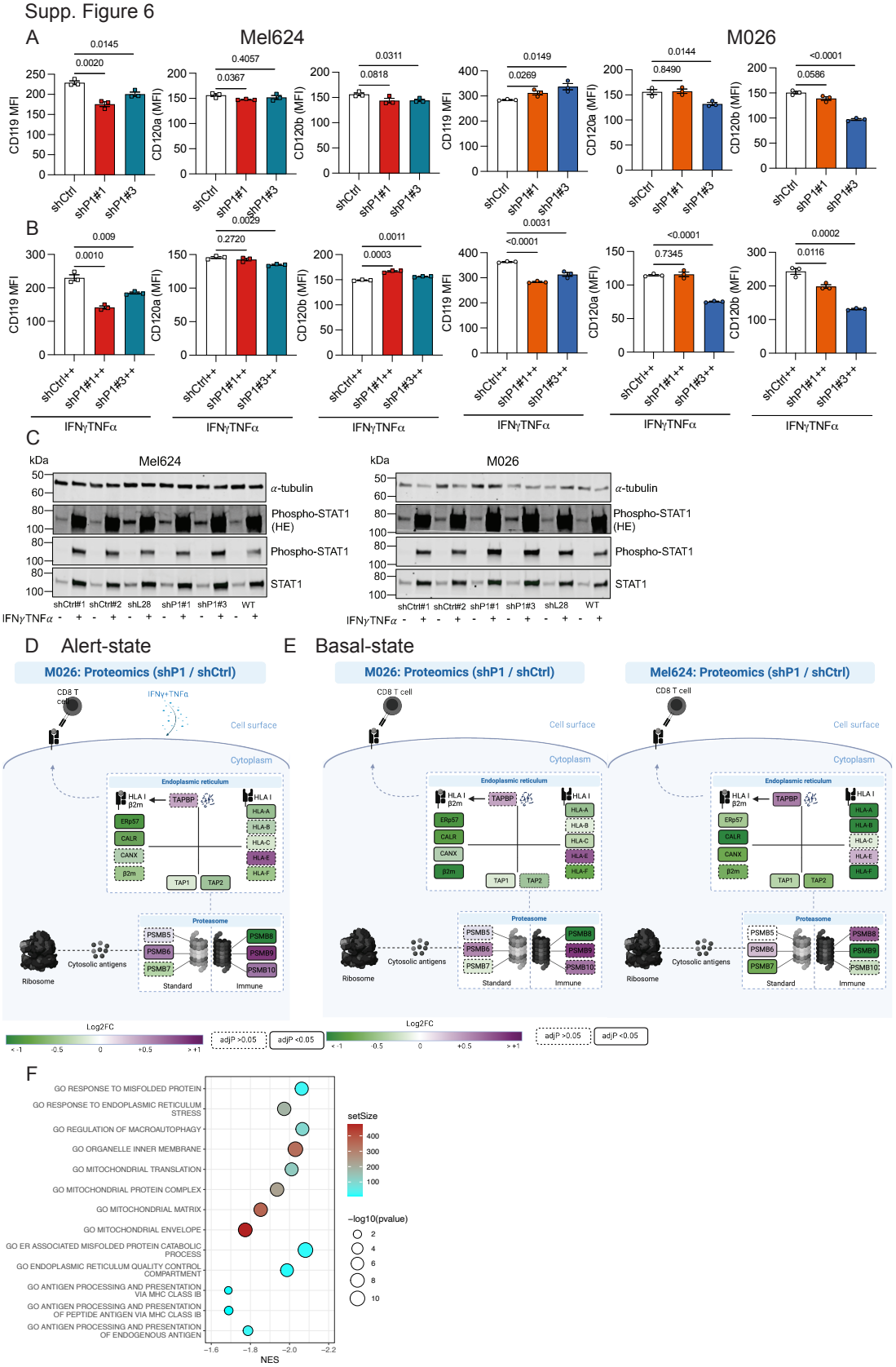

Figure S6. [legend on the next page]

Figure S6 [previous page]. P1 KD attenuates IFNGR1 and TNFR surface levels and decreases APP expression, related to Figure 3

(**A**) IFNGR1, TNFR1, and TNFR2 surface levels are attenuated in shP1 M026 and Mel624 tumor cells. Surface levels were measured by flow cytometry using the MFI. *n* = 3 independent experiments per cell line represented as mean ± SEM. *p* values were calculated using a two-tailed t test.

(**B**) IFNGR1, TNFR1, and TNFR2 surface levels are attenuated in shP1 M026 and Mel624 tumor cells treated with IFNγ/TNF-α. Surface levels were measured by flow cytometry using the MFI. *n* = 3 independent experiments per cell line represented as mean ± SEM. *p* values were calculated using a two-tailed t test.

(**C**) Western blot analysis showing no effect of P1 KD, with our without IFNγ/TNF-α, on STAT1 phosphorylation levels in M026 and Mel624 tumor cells. α-tubulin was used as loading control. *n* = 1 experiment per cell line.

(**D**) Proteomics analysis of the M026 cell line treated with IFNγ/TNF-α (alert-state) reveals downregulation of HLA and other APP components upon P1 KD. *n* = 3 independent experiments, and *p* values were calculated using a two-tailed t test.

(**E**) Proteomics analysis of the M026 and Mel624 cell line (basal-state) reveals downregulation of HLA and other APP components upon P1 KD. *n* = 3 independent experiments, and *p* values were calculated using a two-tailed t test.

(**F**) GSEA of Mel624 cells shows that KD of P1 results in downregulation of genesets associated with antigen presentation. *n* = 3 biological replicates.

Supp. Figure 7

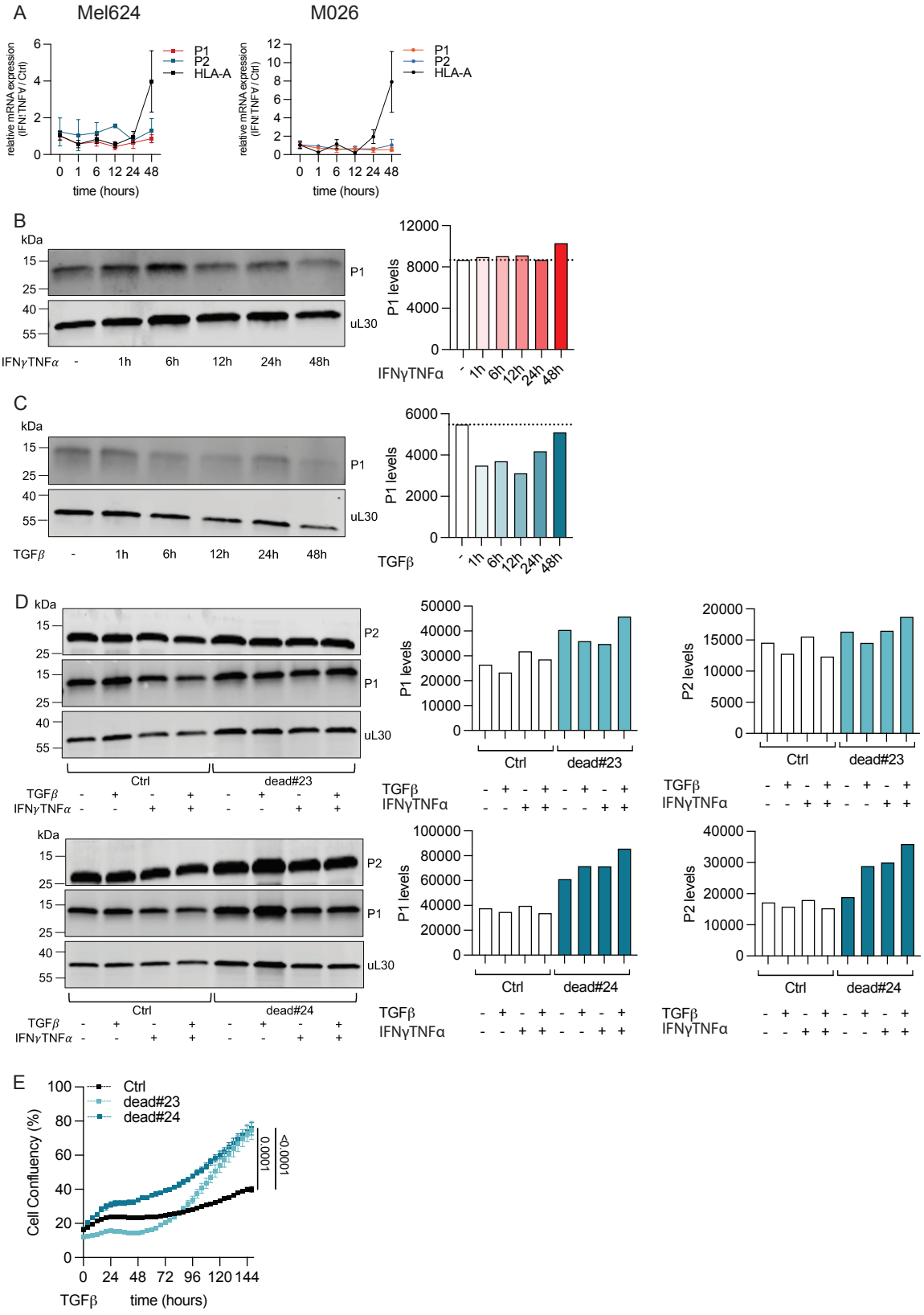

Figure S7. [legend on the next page]

Figure S7 [previous page]. P-stalk phosphorylation inhibits PSR formation, related to Figure 4

(**A**) RT-qPCR analysis confirming *P1* and *P2* are not transcriptionally upregulated upon IFNγ/TNF-α in Mel624 and M026 tumor cells, using *ACTB* as a reference. *HLA-A* expression was used as positive control for IFNγ/TNF-α treatment. *n* = 3 technical replicates represented as mean and error ± SD.

(**B**) Western blot analysis confirming PSR formation after 48 h of IFNγ/TNF-α treatment. Polysomal association of P1 was measured in untreated tumor cells and cells treated with IFNγ/TNF-α at indicated timepoints (1, 6, 12, 24, and 48 h). uL30 was used as control RP for data normalization. *n* = 1 experiment per cell line.

(**C**) Western blot analysis confirming PSR inhibition after 1 h of TGF-β treatment. Polysomal association of P1 was measured in untreated tumor cells and tumor cells treated with TGF-β at indicated timepoints (1, 6, 12, 24, and 48 h). uL30 was used as control RP for data normalization. *n* = 1 experiment per cell line.

(**D**) Western blot analysis of P2 phospho-dead cell lines reveals TGF-β-mediated inhibition of the PSR by phosphorylation. Polysomal association of P1 and P2 was measured in control cells and two phospho-dead cell lines (#23 and #24) with or without TGF-β, IFNγ/TNF-α and IFNγ/TNF-α + TGF-β. uL30 was used as control RP for data normalization. *n* = 1 experiment per cell line.

(**E**) Incucyte LiveCell imaging assay reveals that P2 phospho-dead cell lines are more resistant to chronic TGF-β treatment (0–144 h), underlining the role of P2 phosphorylation in TGF-β-mediated phenotypes. *n* = 6 replicates, and data represent mean and error ± SEM. *p* values were calculated with a two-tailed t test.